

# A global sensitivity analysis of the PlumeRise model of volcanic plumes

Mark J. Woodhouse<sup>a,b</sup>, Andrew J. Hogg<sup>a</sup>, Jeremy C. Phillips<sup>b</sup>

<sup>a</sup>*School of Mathematics, University of Bristol, University Walk, Bristol, BS8 1TW, UK*

<sup>b</sup>*School of Earth Sciences, University of Bristol, Bristol, BS8 1RJ, UK*

---

## Abstract

Integral models of volcanic plumes allow predictions of plume dynamics to be made and the rapid estimation of volcanic source conditions from observations of the plume height by model inversion. Here we introduce PlumeRise, an integral model of volcanic plumes that incorporates a description of the state of the atmosphere, includes the effects of wind and the phase change of water, and has been developed as a freely available web-based tool. The model can be used to estimate the height of a volcanic plume when the source conditions are specified, or to infer the strength of the source from an observed plume height through a model inversion. The predictions of the volcanic plume dynamics produced by the model are analysed in four case studies in which the atmospheric conditions and the strength of the source are varied. A global sensitivity analysis of the model to a selection of model inputs is performed and the results are analysed using parallel coordinate plots for visualisation and variance-based sensitivity indices to quantify the sensitivity of model outputs. We find that if the atmospheric conditions do not vary widely then there is a small set of model inputs that strongly influence the model predictions. When estimating the height of the plume, the source mass flux has a controlling influence on the model prediction, while variations in the plume height strongly effect the inferred value of the source mass flux when performing inversion studies. The values taken for the entrainment coefficients have a particularly important effect on the quantitative predictions. The dependencies of the model outputs to variations in the inputs are discussed and compared to simple algebraic expressions that relate source conditions to the height of the plume.

*Keywords:* Volcanic plumes, Integral model, Web-tool, Global sensitivity analysis

*Preprint submitted to Journal of Volcanology and Geothermal Research February 17, 2016*

---

## 1. Introduction

Volcanic tephra produced during explosive volcanic eruptions is hazardous to populations and infrastructure. Tephra transported in the atmosphere is damaging to aircraft, causing widespread disruption to international air transport, while tephra deposited on the ground has impacts on human health and can cause structural damage to buildings (Jenkins et al., 2015). The largest eruptions can inject large volumes of tephra at stratospheric levels, causing global temperature changes and tephra deposition over thousands of square kilometres (Self, 2006). However, even relatively small eruptions have regional impacts, as fine ash is transported far from the volcanic source by atmospheric winds and buoyancy forces.

The mitigation of the hazard presented by volcanic ash relies on effective forecasting of ash transport in the atmosphere, which requires estimates of source conditions, particularly the maximum height in the atmosphere to which ash is transported (subsequently referred to as the plume height) and the rate at which ash is delivered from the vent (the source mass flux). These quantities are fundamentally related by the dynamics of the volcanic plume. By developing models of volcanic plumes, we can gain insight into the physical processes that control the plume rise and may infer unobserved quantities such as the source mass flux by matching model predictions to observations.

Volcanic plumes are mixtures of solid pyroclasts, produced by the fragmentation of magma in the volcano conduit, with gases exsolved from the magma and entrained from the environment. On ejection from the vent, the mixture is usually hotter and more dense than the surrounding atmosphere and is initially carried upwards by inertia as a jet (Woods, 1988; Sparks et al., 1997). Typically the flow is turbulent on exit from the vent or becomes turbulent close to the vent (Sparks et al., 1997). The turbulent flow field results in a mixing of ambient air with the erupted material, with a transfer of heat and momentum to the entrained air. The expansion of the gaseous phases causes a reduction in the bulk density of the mixture, which may become buoyant before the initial momentum is lost if the entrainment and heat transfer are sufficiently efficient, and the jet transitions into a buoyant plume which can ascend to high altitudes. If insufficient mixing occurs then the mixture does not become buoyant before the vertical momentum is

lost, and the jet collapses (Sparks et al., 1997; Degruyter and Bonadonna, 2013).

In addition to the volcanic source controls on the plume dynamics, the atmosphere also strongly influences the rise of the plume (Woods, 1988; Sparks et al., 1997; Glaze and Baloga, 1996; Bursik, 2001; Woodhouse et al., 2013). A large proportion of the erupted gaseous phase is water vapour derived from magma, and additional water vapour is entrained from the moist troposphere. The plume transports this moisture to higher levels where it can condense to liquid water and ice (Woods, 1993; Glaze et al., 1997; Mastin, 2007). The phase change results in the release of latent heat to the plume and this source of energy can, in some atmospheric and volcanological conditions, promote significant additional rise of the plume (Woods, 1993; Glaze et al., 1997). In contrast, atmospheric winds enhance the mixing of ambient air into the plume, thus more rapidly reducing the density contrast between the plume mixture and the ambient atmosphere, resulting in a reduction in the rise height of the plume (Bursik, 2001; Degruyter and Bonadonna, 2012; Woodhouse et al., 2013), while the additional entrainment due to the wind can lead to plumes that would collapse in a quiescent atmosphere becoming buoyant (Degruyter and Bonadonna, 2013; de' Michieli Vitturi et al., This issue).

The turbulent and multiphase character of volcanic plumes and the large range of scales on which physical processes operate means that simulating all aspects of the motion is computationally demanding. For rapid hazard assessment during a volcanic crisis, simplified models with low computational requirements are valuable tools for producing estimates of the important properties of the volcanic source and the plume. Here we present PlumeRise, an integral model of volcanic plumes that includes descriptions of atmospheric wind and phase changes of water. In addition to use in research, a version of PlumeRise has been developed as a web-tool (figure 1) that can be freely accessed at [www.plumerise.bris.ac.uk](http://www.plumerise.bris.ac.uk) and can be used to examine the source and atmospheric controls on the plume motion and perform model inversions to estimate the source conditions required for the plume to attain a specified height.

The PlumeRise model has 12 dimensional parameters, four boundary conditions that must be specified, and requires profiles of the atmospheric pressure, temperature, wind speed and direction, and the relative humidity. These dimensional model inputs can be formed into 17 dimensionless groups. This high dimensional space of model inputs and the non-linearity

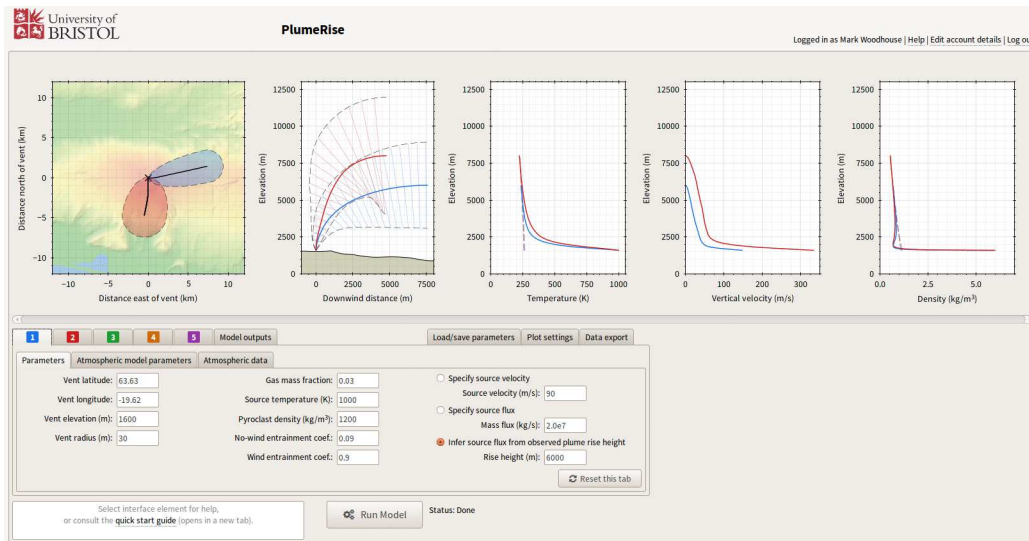


Figure 1: The main settings and results page of the PlumeRise web-tool. Up to five sets of source conditions and atmospheric profiles can be specified in the settings box, and results are displayed in the plots panel. In this example two different atmospheric profiles are used (passed through the “Atmospheric data” tab), and two plume heights are specified using the “Infer source flux from observed rise height” option. An inversion calculation adjusts the source velocity to match the centreline height to the height specified. The plots show a plan-view and cross-section of the plumes, and the temperatures in the plumes and atmospheres, the vertical velocities, and the densities in the plumes and atmospheres as functions of the elevation above sea level. Other plots are available and can be selected in the “Plot settings” tab.

of the system of equations means that it is difficult to anticipate all of the dependencies of the model outputs to the values taken for the input parameters and boundary conditions. Note, in the PlumeRise web-tool some of the parameters are fixed at characteristic values, while the research version that is examined here allows all model inputs to be varied. Small changes in parameter values, and in combinations of parameters, can result in substantial changes to the model output. A crucial question in the application of models to interpret observations is to what extent and accuracy must parameters in the model be calibrated and boundary conditions chosen in order to draw meaningful inferences about the volcanic system? In this study we conduct a global sensitivity analysis of the PlumeRise model to examine the variability of the model predictions when parameter values, boundary conditions, and atmospheric inputs are changed.

This contribution is structured as follows. We present first the system of equations that are solved in the PlumeRise model, and the modelling assumptions on which these are based. We then introduce the methods used for the global sensitivity analysis. The results of the sensitivity analysis performed in four case studies are presented. We then discuss the interpretation of these results, in particular examining how the results compare to the algebraic expressions that relate the plume rise height to the conditions at the volcanic source.

## **2. The PlumeRise model of moist, wind-blown volcanic plumes**

PlumeRise is an integral model of a steady volcanic eruption column in a wind field. Atmospheric conditions are included through profiles of the pressure, temperature, wind speed and direction, and the relative humidity, which can be taken from direct measurement (e.g. radiosonde soundings), numerical weather prediction tools, or constructed to represent typical conditions (e.g. standard atmospheres). The model is derived by combining an integral model of pure plumes in a horizontal wind (Hewett et al., 1971) with an integral model of volcanic eruption columns in a quiescent atmosphere (Woods, 1988). Details of the model development are presented in Woodhouse et al. (2013). Here we present the governing equations and the main assumptions on which the model is based.

A steady model of plumes is appropriate if the time scale of variations in source and atmospheric conditions are much longer than the time of rise of fluid parcels through the atmosphere, the latter time scale given by  $1/N$

where  $N$  is the buoyancy frequency of the atmosphere, with a typical value of  $N = 0.01 \text{ s}^{-1}$  (Gill, 1982). The plume can then be considered to be in a statistically steady state, and the transient turbulent motions are removed by averaging on a time scale that is longer than the eddy turn-over time (Woods, 2010). The turbulent mixing of the ambient fluid into the plume is then represented by a flow into the plume, referred to as entrainment (Morton et al., 1956). The turbulence within the body of the plume ensures the material remains well mixed, and properties of the eruption column can be described by time-averaged bulk quantities. We assume that the radial profiles of the bulk density, axial velocity and temperature in the plume are modelled by top-hat profiles (i.e. these quantities have constant values within the plume and vanish outside the plume boundary) and that cross-sections of the plume normal to the axis are circular with radius  $L$ . The assumption of top-hat profiles is a mathematical convenience; other profiles, for example Gaussian distributions, could be adopted. However, adopting such profiles has little effect on the predictions of plume models in quiescent environments if the value of the no-wind entrainment coefficient is appropriately adjusted (Kaye, 2008). The bulk density of the plume, denoted by  $\rho$ , varies due to the entrainment, mixing and expansion of atmospheric air, which has density  $\rho_A$ . The bulk temperature of the column is denoted by  $T$ , while the atmospheric temperature is  $T_A$ . The plume is composed of gases, derived from the magma and entrained from the environment, solids pyroclasts and liquid water (if conditions allow for the condensed water phase). The mass fraction of gas in the plume is denoted by  $n$ .

While PlumeRise models the transport of solid pyroclasts in the plume, the fallout of pyroclasts is not modelled. Models of the fallout of pyroclasts from the rising plume have been proposed for plumes in quiescent environments (Ernst et al., 1996; Woods and Bursik, 1991; Sparks et al., 1997), and have shown that the loss of mass associated with fallout has only a small effect on the rise height attained by buoyant plumes unless fallout occurs before pyroclasts have reached thermal equilibrium with the gases in the plume (Woods and Bursik, 1991; Sparks et al., 1997). Thermal equilibrium occurs rapidly for small grain sizes, within 1 km of the vent for pyroclasts of diameter up to approximately 0.4 cm ejected at  $100 \text{ ms}^{-1}$  (Woods and Bursik, 1991; Sparks et al., 1997). Therefore the fallout of pyroclasts has little effect on fine-grained eruption columns. However, fallout may be an important process for eruptions that produce larger pyroclasts for which the relaxation time to thermal equilibrium is longer and so pyroclasts may fall out before

thermal equilibrium is reached, reducing the supply of heat (and therefore buoyancy) to the eruption column (Woods and Bursik, 1991; Sparks et al., 1997). It is not currently known how the interaction with the wind modifies the empirical settling models (Ernst et al., 1996; Bursik, 2001) that are used to describe sedimentation of particles from plumes rising in quiescent environments, but we expect fine-grained pyroclasts to rapidly reach thermal equilibrium with the gases in a wind-blown plume, and therefore to have only a secondary effect on the rise height attained by the plume.

The moisture content of an eruption column is included by accounting for phase changes of the water within the column and the effect of phase changes on the energy budget (Morton, 1957; Woods, 1993; Koyaguchi and Woods, 1996; Mastin, 2007). For simplicity, we neglect the phase changes of water vapour and liquid water to ice, as the latent heat of freezing is about a factor of 10 smaller than the latent heat of vaporisation (Sparks et al., 1997) so a description of condensation alone is likely to be sufficient in the majority of settings, and the complexities of ice formation in volcanic plumes is not fully understood.

Our model assumes that the pressure in the plume is equal to the atmospheric pressure throughout the ascent. This assumption is appropriate for slender plumes (Morton et al., 1956; Woods, 1988; Linden, 2000), where the length scale of radial variations is much smaller than the length scale for vertical variations. The assumption may not be appropriate very near to the vent, where the erupted material can have a substantial over-pressure (Woods and Bower, 1995; Ogden et al., 2008b; Saffaraval et al., 2012). This alters the flow dynamics (Woods and Bower, 1995; Ogden et al., 2008b,a), in particular the turbulent mixing processes, such that a different parameterization of entrainment is required (Saffaraval et al., 2012). However, the pressure in the near vent jet rapidly adjusts to atmospheric pressure (Saffaraval et al., 2012) and therefore we expect the model results to be little affected by the simplified description (Saffaraval et al., 2012).

The entrainment of ambient air into the body of the plume through the action of turbulent eddies is parameterized by an entrainment velocity that is directed normal to the local plume axis (figure 2). In a windy environment we adopt the parameterization of Hewett et al. (1971),

$$U_e = k_s |U - V \cos \theta| + k_w |V \sin \theta|, \quad (1)$$

where  $U$  is the axial centreline velocity of the plume,  $V$  is the horizontal velocity of the wind,  $\theta$  is the local angle on the plume axis to the horizontal,

$k_s$  is the entrainment coefficient due to the motion of the plume relative to the environment, and  $k_w$  is the entrainment coefficient due to the alignment of the wind field with the local normal to the plume axis. In the absence of atmospheric wind,  $V \equiv 0$ , the entrainment velocity (1) reduces to  $U_e = k_s U$ , and therefore  $k_s$  is the entrainment coefficient for plumes rising in a quiescent environment (Morton et al., 1956; Woods, 1988). We therefore refer to  $k_s$  as the no-wind entrainment coefficient, and  $k_w$  as the wind entrainment coefficient. (Note  $k_s$  is given the symbol  $\alpha$  and  $k_w$  the symbol  $\beta$  in Costa et al. 2016.)

It is often assumed that the entrainment coefficients take constant values, and experiments on plumes in a quiescent ambient show that this is appropriate when the radial profiles of plume properties reach a self-similar form (Papanicolaou and List, 1988; Ezzamel et al., 2015). However, close to the source there is a deviation from the self-similar plume profile as the flow is momentum-driven as it exists the vent (Kaminski et al., 2005; Papanicolaou and List, 1988; Ezzamel et al., 2015). Non-constant forms for the no-wind entrainment coefficient have been proposed (Wang and Law, 2002; Kaminski et al., 2005; Carazzo et al., 2006; Folch et al., 2015) for quiescent settings, but there has been no investigation of the detailed influence of the wind on the variation of the entrainment coefficients. In PlumeRise we adopt a simple model (Woods, 1988) of the variation of the entrainment coefficient as the eruption column develops from a momentum-driven jet near the vent to a buoyant plume, with the eruption column separated into a near-source jet-like region (also referred to as the gas-thrust region) and a buoyant plume-like region. In the near-source region the density of the erupted mixture is much greater than that of the atmosphere, and the entrainment coefficient is taken to be a function of the density contrast (Woods, 1988) with  $k_s = \sqrt{\rho/\rho_A}/16$ , where  $\rho$  is the bulk density of the eruption column and  $\rho_A$  is the density of the atmosphere. If the eruption column become buoyant, we take the entrainment coefficient to be constant with  $k_s = 0.09$  in the buoyant region. It is not known how the wind-entrainment coefficient varies in the transition from jet-like to plume-like behaviour, so we take a constant entrainment coefficient  $k_w = 0.9$  determined from a series of laboratory experiments (Hewett et al., 1971).

A mathematical description of the variation of the steady eruption column with distance from the volcanic source is formulated in a plume-centred coordinate system within a Cartesian frame of reference (figure 2). We let  $z$  denote the height of the plume,  $x$  and  $y$  denote the Cartesian coordinates

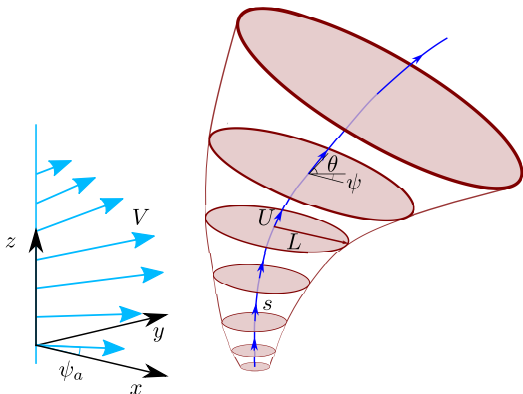


Figure 2: The coordinate system for the PlumeRise model. A Cartesian coordinate system is fixed with  $x$  denoting the East-West (longitudinal) coordinate,  $y$  denoting the North-South (latitudinal) coordinate and  $z$  denoting the vertical coordinate (altitude). Equations describing the plume dynamics are derived in a plume-centred coordinate system, with  $s$  denoting the curvilinear distance (arclength) from the vent along the plume axis,  $\theta(s)$  denoting the angle of the centreline with respect to the horizontal, and  $\psi$  the angle of the trajectory in the  $xy$ -plane. A cross-section of the plume normal to the centreline is circular with radius  $L(s)$ . The centreline speed of the plume is denoted by  $U(s)$ . The wind speed is denoted by  $V(z)$ , with the angle  $\psi_a$  denoting the angle to which the wind blows.

orthogonal to  $z$ , and  $s$  denote the curvilinear distance from the vent along the centreline of the plume. Therefore  $x$ ,  $y$  and  $z$  are related to  $s$  through

$$\frac{dx}{ds} = \cos \theta \cos \psi, \quad \frac{dy}{ds} = \cos \theta \sin \psi, \quad \frac{dz}{ds} = \sin \theta. \quad (2)$$

Equations describing the variation of the plume density  $\rho(s)$ , radius  $L(s)$ , centreline velocity  $U(s)$ , and temperature  $T(s)$  are derived by considering conservation of mass, momentum and energy in cross-sections normal to the plume axis (Woodhouse et al., 2013). The mass of the column increases due to the entrainment of atmospheric air, so that from conservation of mass we have

$$\frac{d}{ds} (\rho U L^2) = 2\rho_A U_e L, \quad (3)$$

noting that the fallout of solid pyroclasts is neglected. The mass flux through a cross section normal to the plume centreline is given by

$$Q = \pi \rho U L^2. \quad (4)$$

An equation for the conservation of vertical momentum can be written using Newton's second law, with the change in vertical momentum balancing the

buoyancy force,

$$\frac{d}{ds} (\rho U^2 L^2 \sin \theta) = (\rho_A - \rho) g L^2. \quad (5)$$

Here it is assumed that non-hydrostatic pressure gradients and stresses are negligible, assumptions which are justified based on the relative slenderness of the plume. The horizontal momentum of the column changes only due to the entrainment of fluid from the windy environment, so conservation of momentum in the  $x$  and  $y$  directions can be written as

$$\frac{d}{ds} (\rho U^2 L^2 \cos \theta \cos \psi) = 2\rho_A U_e L V \cos \psi_A, \quad (6)$$

$$\frac{d}{ds} (\rho U^2 L^2 \cos \theta \sin \psi) = 2\rho_A U_e L V \sin \psi_A, \quad (7)$$

respectively, where  $\psi_A$  is the angle of the wind vector from the axis  $x = 0$ .

The conservation of energy in the plume equates the change in total energy (given by the sum of the bulk enthalpy, kinetic energy and potential energy) in the plume to the total energy of the fluid entrained from the atmosphere and the energy released when water changes phase in the plume. This is expressed symbolically as

$$\begin{aligned} \frac{d}{ds} \left( \rho U L^2 \left( C_p T + \frac{U^2}{2} + gz \right) \right) &= 2\rho_A L U_e \left( C_A T_A + \frac{U_e^2}{2} + gz \right) \\ &+ L_{c0} \frac{d}{ds} \left( \rho L^2 U (\phi - \phi_v) \right), \end{aligned} \quad (8)$$

where  $C_p$  and  $C_A$  are the specific heat capacities at constant pressure of the bulk plume and the atmospheric air, respectively,  $\phi$  is the mass fraction of liquid water and water vapour in the column, and  $\phi_v$  is mass fraction of water vapour in the column. Note, in (8) turbulent dissipation is neglected. In modelling the condensation of water vapour in equation (8), the latent heat of condensation,  $L_c(T)$  (measured in  $\text{J kg}^{-1}$ ), is approximated by

$$L_c(T) = L_{c0} + (C_v - C_w) (T - 273), \quad (9)$$

for temperature,  $T$ , measured in Kelvin, where  $L_{c0} = 2.5 \times 10^6 \text{ J kg}^{-1}$  is the latent heat of vaporisation at 273 K (Rogers and Yau, 1989), and  $C_v$  and  $C_w$  are the specific heat capacities at constant pressure of water vapour and liquid water, respectively, measured in  $\text{J K}^{-1} \text{ kg}^{-1}$ .

We assume that the gas released at the vent is composed entirely of water vapour released from magma in the conduit and water vapour from the evaporation of ground water. Water vapour is entrained into the eruption column from the moist atmosphere and is advected with the bulk flow. Therefore conservation of water in the column can be written as

$$\frac{d}{ds} (\phi \rho U L^2) = 2 \rho_A U_e L \phi_A, \quad (10)$$

where  $\phi_A$  is the mass fraction of water vapour in the atmosphere (i.e. the specific humidity of the atmosphere).

Condensation is assumed to occur rapidly once the eruption column has become saturated with respect to water vapour, such that the column remains saturated. Thus, once saturated, the mass fraction of gas in the column which is composed of water vapour, denoted by  $w$ , remains at a value such that the partial pressure of water vapour,  $P_v$ , is equal to the saturation vapour pressure in the column,  $e_s(T)$ , so  $P_v = e_s(T)$  (Koyaguchi and Woods, 1996). Note,  $\phi_v = nw$  where  $n$  is the mass fraction of gas (dry air and water vapour) in the column. Assuming the gas phase is a mixture of water vapour and dry air, and each component can be considered an ideal gas, the partial pressure of water vapour is given by

$$P_v = w \frac{\rho_g}{\rho_v} P_A = \frac{w R_v}{w R_v + (1 - w) R_a} P_A, \quad (11)$$

where  $\rho_g$  is the density of the gas phase,  $\rho_v$  is the density of water vapour,  $R_v$  and  $R_a$  are the specific gas constants of water vapour and dry air, respectively, and  $P_A$  is the pressure in the column which is assumed to adjust instantaneously to the local atmospheric pressure. Here we adopt an empirical approximation for the saturation vapour pressure (Alduchov and Eskridge, 1996):

$$e_s(T) = 610.94 \exp \left( \frac{17.625 (T - 273.15)}{T - 30.01} \right), \quad (12)$$

for temperature,  $T$ , measured in Kelvin.

The bulk density of the column is given by

$$\frac{1}{\rho} = \frac{n}{\rho_g} + \frac{\phi_w}{\rho_w} + \frac{1 - n - \phi_w}{\sigma}, \quad (13)$$

where  $\rho_w$  is the density of liquid water (assumed constant in the atmosphere) and  $\phi_w = \phi - \phi_v$  is the mass fraction of liquid water in the plume. The density

of the gas phase is given by

$$\rho_g = \frac{P_a}{R_g T}, \quad (14)$$

where the bulk gas constant of the column is given by

$$R_g = wR_v + (1 - w)R_a. \quad (15)$$

The bulk specific heat capacity at constant pressure is

$$C_p = nC_g + \phi_w C_w + (1 - n - \phi_w) C_s, \quad (16)$$

where  $C_s$  is the specific heat capacity at constant pressure of the solid pyroclasts, and  $C_g = wC_v + (1 - w)C_a$  is the specific heat capacity at constant pressure of the gas phase, with  $C_A$  denoting the specific heat capacity at constant pressure of dry air.

The system of equations is augmented by boundary conditions that prescribe conditions at the volcanic vent. PlumeRise requires the specification of two of the source mass flux  $Q_0$ , the source momentum flux  $M_0$ , the radius of the vent  $L_0$  and the exit velocity  $U_0$ . Additionally, the magmatic temperature at the vent  $T_0$ , the mass fraction of gas at the vent  $n_0$  and the altitude of the vent  $z_0$  are required.

The system of equations are solved numerically using a fourth-order Cash-Karp Runge-Kutta scheme with automated step-size adjustment for error control (Press et al., 2007). The algebraic equations are differentiated to produce a coupled system of fourteen ordinary differential equations that can be efficiently integrated numerically.

Typically the atmospheric profiles have a much coarser vertical resolution than the steps taken in the numerical integration. The atmospheric profiles are therefore interpolated, with linear interpolation for all fields except the atmospheric pressure for which an exponential form is used to reproduce the expected hydrostatic pressure profile in the atmosphere (Gill, 1982). There are occasions where the atmospheric data do not extend to the height reached by the plume. In this case the atmospheric fields are extrapolated using spatially constant values, with the exception of the pressure field for which an exponential function is used. The extrapolation of the atmospheric data introduces significant uncertainty into the model predictions if the plume rises to altitudes above levels at which atmospheric data is given.

The integral plume model has short execution times, with ‘forward’ model evaluations (i.e. an integration from specified initial conditions to the point

of maximum rise) taking less than 0.5 s on a desktop computer. The model is therefore well suited for use in rapid hazard assessment, and to facilitate this use of the model during volcanic crises, we have developed the PlumeRise web-tool. The web-tool is freely available at [www.plumerise.bris.ac.uk](http://www.plumerise.bris.ac.uk). A screen-shot of the main page of the web-tool is shown in figure 1.

The ‘inverse’ problem of determining the source mass flux by matching the plume height to a specified value can be solved by iteratively adjusting the source conditions and performing forward model runs. We note that there is not necessarily a unique solution of the inverse problem, as variations in one of the source conditions can be compensated by changes in another. Woodhouse et al. (2013) and Woodhouse and Behnke (2014) used a simple inversion strategy, in which a single source boundary value was adjusted, to estimate the source mass flux from observations of the plume height. However, these studies did not carefully consider uncertainty in the observations and the model formulation. Woodhouse et al. (2015) demonstrated that uncertainty in observations and model parameters strongly constrains the inferences that can be made from inversion studies.

The possibility of column collapse, where there is insufficient mixing of ambient air to allow the initially dense jet to become buoyant before the vertical momentum of the material ejected at the vent is expended, means that there is not always a solution of the inverse problem. In the PlumeRise web-tool we implement an inversion scheme, adjusting the exit velocity for a specified vent radius to vary the source mass flux. In this study, the exit velocity is specified so the vent radius is adjusted in the inversion calculation. To assess the possibility of column collapse, we first perform forward model evaluations on a coarse sample of points across a wide range of the exit velocity, which indicates whether a solution is possible, and then use bisection to refine the source estimate. The rapid forward evaluations means that the inversion calculation typically completes in a few seconds.

### **3. Methods for the analysis of sensitivity of the PlumeRise model**

For nonlinear mathematical models with numerous inputs it is often difficult to anticipate the response of the model output to changes in the inputs. Complicated interactions of physical processes mean that varying one input parameter at a time does not adequately characterise the range of model outputs that are possible, although the one-at-a-time analysis may be valuable as a preliminary screening exercise. A comprehensive sensitivity analyses

must examine the response of the model to changes in all parameters across their range of values; this is known as global sensitivity analysis (Saltelli et al., 2008).

The PlumeRise model can be considered as a function that maps a set of input values onto a set of outputs, written symbolically as

$$\mathbf{y} = \mathbf{f}(\mathbf{x}; \boldsymbol{\theta}), \quad (17)$$

where  $\mathbf{y}$  is a vector of model outputs,  $\mathbf{x}$  is a vector of model inputs,  $\boldsymbol{\theta}$  is a vector of model parameter values, and  $\mathbf{f}$  is a vector function representing the PlumeRise model. The model inputs,  $\mathbf{x}$ , in the PlumeRise model are the boundary conditions for the system of ordinary differential equations that represent the conditions at the volcanic vent. In addition, the model requires the specification of a number of parameter values that characterise the physical properties and processes that occur in the volcanic plume. For examples, parameters are required to characterise the turbulent mixing and the thermodynamic properties of the constituent phases in the plume. Furthermore, there are additional inputs into the model that determine the solutions. In particular in the PlumeRise model, profiles representing the state of the atmosphere are required. In Woodhouse et al. (2015) we refer to the atmospheric profiles as the ‘model forcing’ as these inputs are typically fixed, as is the uncertainty they introduce into the model predictions. Here, in our abstraction of the model, we include the model forcing as a member of the set of model parameters.

As part of the eruption column model inter-comparison exercise (Costa et al., 2016), we have performed a sensitivity analysis of the PlumeRise model to a subset of the model inputs as specified by the exercise facilitators. The exercise required the assessment of the sensitivity of the model outputs to a range of model inputs and parameters. Some of these inputs can take values on a continuous interval, while others are discrete ‘switches’ that determine whether some physical processes are included in the model. For convenience, we reclassify the inputs to the model as described in equation (17); the model inputs  $\mathbf{x}$  will henceforth refer to the set of boundary conditions and parameters that are varied in the sensitivity analysis, while the inputs  $\boldsymbol{\theta}$  will denote the set of parameter values and atmospheric profiles that held fixed in the analysis. Table 1 gives the model inputs that are examined in this study.

To examine the sensitivity of the model to changes in the wind speed, a wind speed scale factor (denoted by  $\lambda$ ) is introduced. The wind speed input

Table 1: Model inputs varied in the sensitivity analyses. For inputs that can vary continuously, the range of parameter values for the weak and strong plume cases are given.

Parameter (symbol)	Range of values	
	Weak eruption	Strong eruption
No-wind entrainment coefficient ( $k_s$ )	0.05–0.15	0.05–0.15
Wind entrainment coefficient ( $k_w$ )	0.1–1.0	0.1–1.0
Source mass flux ( $Q_0$ )	$3 \times 10^5$ – $7.5 \times 10^6$ kg/s	$3 \times 10^8$ – $7.5 \times 10^9$ kg/s
Plume height ( $H_{\text{top}}$ )	6–9 km	30.8–46.2 km
Exit velocity ( $U_0$ )	94.5–175.5 m/s	192.5–357.5 m/s
Source temperature ( $T_0$ )	1173–1373 K	953–1153 K
Source gas mass fraction ( $n_0$ )	0.01–0.05	0.03–0.07
Wind scale factor ( $\lambda$ )	0.8–1.2	0.8–1.2
Phase change of water	‘on’ or ‘off’	‘on’ or ‘off’
Atmospheric moisture	‘on’ or ‘off’	‘on’ or ‘off’

into the model is then taken as  $\lambda V(z)$  where  $V(z)$  is the measured wind speed. We also consider cases where the wind is removed from the model inputs (i.e. we fix  $\lambda = 0$ ). When  $\lambda = 0$  the wind entrainment coefficient  $k_w$  and the wind speed scale factor  $\lambda$  do not influence the model results, and can therefore be removed from the analysis.

In the sensitivity study reported in the inter-comparison exercise, the model output was a scalar quantity, and we denote this output by  $y$  in the abstraction of the model. However, two modes of application of the model were required: (i) ‘forward modelling’ where the source mass flux (mass eruption rate) at the vent was specified and the primary model output was the plume height, taken to be the maximum height of the centreline of the plume, at which point the vertical component of the velocity at the plume centreline vanishes; (ii) ‘inverse modelling’ where the plume height was specified and a model inversion was required to determine the source mass flux.

We note that, as there are inputs to the model that are not varied in this analysis, this study should be considered as partial sensitivity analysis. In particular, the parameters that specify the physical and thermodynamic properties of the constituent phases of the plume are not varied from specified values. However, these parameters are uncertain in applications, and in Woodhouse et al. (2015) we demonstrated that variations in the thermodynamic parameters can strongly influence the model output, with the changes in the specific heat capacity of solid pyroclasts effecting the variance of the model outputs to a similar extent as the entrainment coefficients. Further-

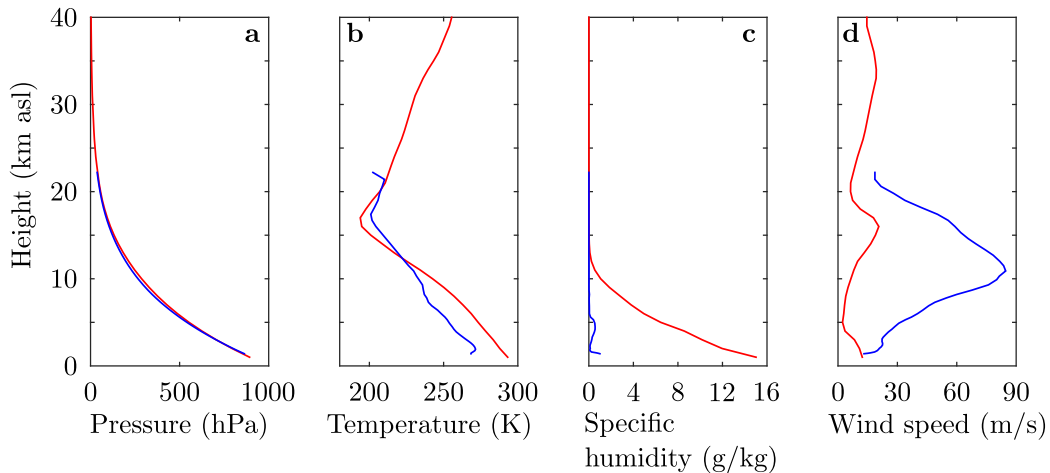


Figure 3: Meteorological conditions for the weak (blue) and strong (red) eruption cases, with **a** pressure, **b** temperature, **c** specific humidity and **d** wind speed as functions of the height above sea level.

more, there are boundary conditions that are fixed in the analysis, and the profiles of the atmospheric conditions are not varied (with the exception of a scaling of the wind speed). To examine the effect of these constraints, two case studies were considered, representing an eruption with a relatively low source mass flux (referred to as a ‘Weak eruption’) and an eruption with a relatively high source mass flux (referred to as a ‘Strong eruption’), with different atmospheric conditions for each case (figure 3). We note in particular that the atmospheric profile used in the weak eruption has much higher wind speeds than the profile for the strong eruption, but that the water vapour loading of the atmosphere is substantially greater for the strong eruption. Details of these case studies and their meteorological conditions are given in Costa et al. (2016).

A challenge in global sensitivity analysis is to provide summaries of the variation in the model outputs as the input parameters are varied. Here we take two approaches. We display graphically the dependencies of the model outputs on the input parameters using parallel coordinates plots (Wegman, 1990), a useful visualisation method for multidimensional data. To quantify the sensitivity of the outputs of the model to variations in the input parameters we use variance-based sensitivity indices that provide summary statistics.

### 3.1. *Parallel coordinates plots*

Visualising a function of many variables is challenging. For a function of a single variable, plotting the independent and dependent variables on orthogonal Cartesian coordinate axes is ubiquitous, and the interpretation of the resulting plot is usually straight-forward. The use of Cartesian coordinate axis is also possible for functions of two variables, although we often must carefully select appropriate projections of the three-dimensional space onto the two dimensions of the page. For functions with more than two independent variables, the use of orthogonal Cartesian coordinates is more problematic. In some cases we can identify variables that allow us to reduce the dimension of the visualisation (for example, using contours to represent a three-dimensional surface on a two-dimensional plane), but as the number of variables increases the difficulties in using orthogonal coordinate axes grows.

An alternative approach is to arrange the coordinate axis in parallel, known as parallel coordinate plots (Wegman, 1990). By connecting points on the parallel coordinates with line segments, a trajectory through the coordinates axes demonstrates the relationship between the variables, and plotting a sequence of trajectories allows the dependencies in the model to be examined. It can be shown that no information is lost when a parallel coordinates plot is used in place of orthogonal Cartesian coordinates (Wegman, 1990). Furthermore, the parallel coordinates plots allow multiple dependent variables to be examined together. Examples of parallel coordinates plots are given in Appendix A.

Parallel coordinate plots are useful for visualisation in global sensitivity analyses, as the dependencies of several model outputs on multiple simultaneously varying inputs can be examined. Wegman (1990) gives a detailed introduction to the interpretation of parallel coordinate plots. When inspecting parallel coordinate plots, the eye is often drawn to connections between neighbouring axes. This gives prominence to first-order (and, to a lesser extent, second-order) interactions. As an abstract example, if we denote the three inputs to a model by  $x_1$ ,  $x_2$  and  $x_3$  and the output by  $y$ , and make a parallel coordinates plot with the axes in this order, then it is easy to infer the dependence of  $y$  on  $x_3$  (i.e. the first-order interaction of  $x_3$  and  $y$ ), while we must make more effort to trace trajectories through the coordinate axes to examine the dependence of  $y$  on  $x_1$ . By permuting the ordering of the axes so that each of the model input axes is a neighbour of the output axis, we can more easily recognise the first-order dependence of the model output to variations of the inputs. Here we use the permutation algorithm of

Wegman (1990). In addition, colouring the line segments assists in the visualisation. Examples of parallel coordinate plots, with coloured line segments and permuted ordering of the axes are shown in figures 5–8, 10, 11, 13 and 14.

### 3.2. Variance-based sensitivity indices

The difficulty in visually representing the sensitivity for models with large numbers of inputs motivates the construction of summary statistics. Numerous methods have been proposed to summarise the results of global sensitivity analyses (Saltelli et al., 2008; Pianosi et al., 2015) and here we adopt variance-based sensitivity indices (Sobol’, 2001; Saltelli et al., 2010) as these have been widely used and are relatively easy to compute. In this approach, the variance in the model output is decomposed into contributions from changes in individual input parameters, pair-wise interactions (i.e. two input parameters varying simultaneously) and the sets of higher-order interactions (Sobol’, 2001). Normalised measures, called sensitivity indices, are calculated. While the sensitivity indices are often useful summary statistics, the characterisation of the sensitivity of the model through the variance of the model output can be misleading if the distribution of model outputs is highly skewed or multi-modal (Pianosi et al., 2015).

The first-order sensitivity index, denoted by  $S_i$  for model input  $x_i$  where the index  $i = 1 \dots N$  with  $N$  denoting the number of elements of the vector  $\mathbf{x}$  (i.e. the number of inputs to the model that are varied in the sensitivity analysis), is given (in the notation of Saltelli et al. 2010) by

$$S_i = V_{x_i} (E_{\mathbf{x}_{\sim i}} (y|x_i)) / V(y), \quad (18)$$

where  $\mathbf{x}_{\sim i}$  denotes the set of all model inputs excluding  $x_i$ ,  $E_{\mathbf{x}_{\sim i}} (y|x_i)$  represents the expected value of  $y$  taken over all possible values of  $\mathbf{x}_{\sim i}$  with  $x_i$  fixed,  $V_{x_i}$  denotes the variance taken over all values of the input  $x_i$ , and  $V(y)$  is the variance in the model output when all inputs are varied (Saltelli et al., 2010).  $S_i$  is a normalised measure (i.e.  $0 \leq S_i \leq 1$ ) of the effect of the variation of the input  $x_i$  marginalising the effect of other inputs on the model output (Saltelli et al., 2010), which we subsequently refer to as a first-order dependence. Equivalently,  $S_i$  quantifies the expected reduction in variance in the model output that would be achieved if the input  $x_i$  were fixed (Saltelli et al., 2010). Second-order sensitivity indices are normalised measures of the contribution to the variance in model output due to variations in

a pair of parameters; higher order sensitivity indices are similarly constructed (Sobol', 2001). As the number of sensitivity indices grows exponentially with the number of model parameters, rather than compute the sensitivity indices of second-order and higher, it is typical to compute instead the total effects indices (Saltelli et al., 2010).

The total effects index of model input  $x_i$ , denoted by  $S_{Ti}$ , is given by (Saltelli et al., 2008, 2010)

$$S_{Ti} = E_{\mathbf{x}_{\sim i}} (V_{x_i}(y|\mathbf{x}_{\sim i})) / V(y) = 1 - V_{\mathbf{x}_{\sim i}} (E_{x_i}(y|\mathbf{x}_{\sim i})) / V(y), \quad (19)$$

where  $V_{x_i}(y|\mathbf{x}_{\sim i})$  and  $E_{x_i}(y|\mathbf{x}_{\sim i})$  are the variance and expectation, respectively, of the model output taken over all values of the input  $x_i$  with the other inputs fixed, and  $E_{\mathbf{x}_{\sim i}}$  and  $V_{\mathbf{x}_{\sim i}}$  are the expectation and variance, respectively, taken over all inputs except  $x_i$  (Saltelli et al., 2010).  $S_{Ti}$  is a normalised measure ( $0 \leq S_{Ti} \leq 1$ ) of the total contribution from variation in  $x_i$  (first-order and higher-order effects) to the variance in the model output (Saltelli et al., 2010). Equivalently,  $S_{Ti}$  measures the expected variance in model outputs that would remain if all inputs other than  $x_i$  are fixed (Saltelli et al., 2010). The variance-based sensitivity indices allow the variation in the model output to be apportioned to the model inputs, but additional analysis and visualization must be performed to understand the distribution and overall uncertainty of the model outputs.

The calculation of the sensitivity indices requires the evaluation of multi-dimensional integrals over the model input space, and is therefore computationally expensive for a model with a large number of inputs. Saltelli et al. (2010) gives estimators of the integrals required to compute the sensitivity indices that can be obtained from a random, space-filling sampling of the parameter space. Here we use a Latin hypercube design with a maximin criteria, iteratively adjusting the placement of sampling points in the Latin hypercube to maximize the minimum distance between points (Morris and Mitchell, 1995). The model inputs in each sample are drawn from uniform distributions defined on the intervals given in table 1. Confidence intervals on the first-order and total effect sensitivity indices are estimated by a bootstrap of the Latin hypercube samples (Archer et al., 1997; Yang, 2011).

The convergence of the sensitivity indices (particularly the first-order indices) corresponding to model inputs with little influence (i.e. when  $S_i \ll 1$  and  $S_T \ll 1$ ) can be extremely slow. As these inputs are of little further interest we are content to leave unconverged values of the sensitivity indices

where they do not prevent the identification of the model inputs that strongly influence the model. The forward model applications (case i) are computationally cheap and therefore large sample sizes (in excess of 100000 points in the Latin hypercube) are used. In contrast, the model inversion calculations (case ii) require several forward model evaluations (typically around 20 evaluations), and therefore the computational cost increases. We therefore take smaller samples of 10000 points in the Latin hypercube for case (ii) but assess the convergence of the estimators of the sensitivity indices.

## 4. Results

### 4.1. Weak eruption with wind

We consider first the weak eruption scenario with the atmospheric wind included in the atmospheric profiles. The PlumeRise model results using the specified ‘reference’ model inputs are shown in figure 4. For case (i) the source mass flux is fixed at  $Q_0 = 1.5 \times 10^6$  kg/s and the plume top height is found to be  $H = 3.27$  km above the vent which is 1.5 km asl. For case (ii) the plume top height is fixed at  $H = 6$  km above the vent and the source mass flux is found to be  $Q_0 = 1.08 \times 10^7$  kg/s using the reference values for model inputs.

The influence of variations in the model inputs on the plume top height when the source mass flux  $Q_0$  is specified is visualised in a parallel coordinates plots in figure 5. A relatively small sample of 50 inputs sets is drawn using a Latin hypercube design, as taking larger samples results in plots that are more difficult to display. However, the dependencies displayed are consistent with those found when larger samples are used. Each trajectory corresponds to one set of inputs (the entrainment coefficients  $k_s$  and  $k_w$ , exit velocity  $U_0$ , magmatic temperature  $T_0$ , volatile mass fraction  $n_0$ , wind speed scale factor  $\lambda$ , and the source mass flux  $Q_0$ ) from the sample, and the corresponding model outputs which in this case are the plume top height  $H$  and additionally the height at which condensation occurs in the plume (denoted by  $H_c$ , with  $H_c = 0$  if no condensation of water vapour occurs). The trajectories are coloured using the value for the source mass flux.

Figure 5 demonstrates a strong dependence of the model prediction of the plume height  $H$  on the value taken for the source mass flux  $Q_0$ , with larger values of  $H$  when  $Q_0$  has values at the upper end of the specified range. Indeed, the colour scale on the  $H$ -axis is almost reproduced on the  $Q_0$  axis. Therefore there is a strong first-order dependence of  $H$  on  $Q_0$ .

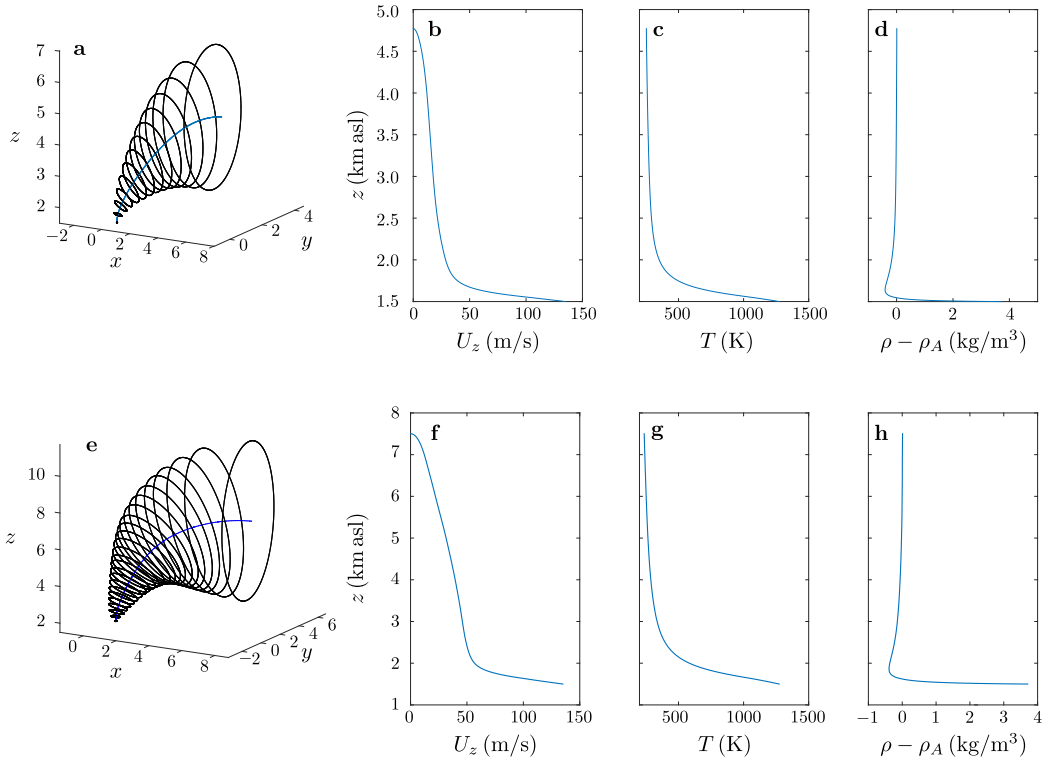


Figure 4: Solutions of the PlumeRise model with the reference input values for the weak eruption scenario. The vent is specified to be at an altitude of 1.5 km asl. In **a–d** the source mass flux is set at  $Q_0 = 1.5 \times 10^6$  kg/s (case i). In **e–h** the plume height is specified to be  $H = 7.5$  km asl (case ii). **a** and **e** illustrate the plume trajectory and radius. The vertical velocity (**b** and **f**), plume temperature (**c** and **g**), and the density difference between the plume and atmosphere (**d** and **h**) as functions of the elevation above sea level are shown.

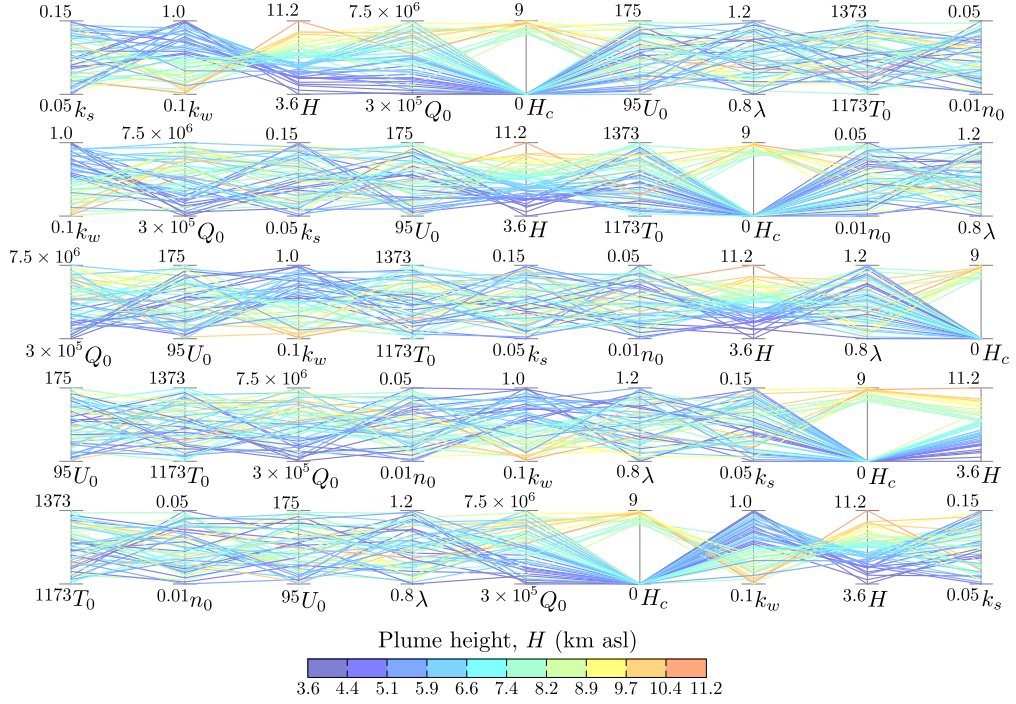


Figure 5: Parallel coordinates plots for the weak eruption case with wind included and the source mass flux specified. The entrainment coefficients  $k_s$  and  $k_w$ , exit velocity  $U_0$  (measured in m/s), magmatic temperature  $T_0$  (K), volatile mass fraction  $n_0$ , wind speed scale factor  $\lambda$ , and the source mass flux  $Q_0$  (kg/s) are varied using a Latin hypercube design with 50 sampling points. The plume height  $H$  (km) is calculated. Note  $Q_0$  is plotted on a logarithmic scale. The height at which condensation occurs in the plume,  $H_c$  (km), is also plotted, with  $H_c = 0$  if no condensation occurs. Trajectories through the coordinate axis represent individual model evaluations, and these are coloured using the plume height  $H$ . In each row, the same numerical output is plotted but the ordering of the axes are permuted to aide with the visual interpretation of the sensitivity to input values.

Similarly, there is a strong first-order dependence of  $H$  on the value of the wind entrainment coefficient  $k_w$ , with larger values of  $H$  predicted when  $k_w$  takes values at the lower end of the range. The line segments connecting the  $k_w$  and  $H$  axes form an "X" and the colour scale on the  $H$ -axis is inverted on the  $k_w$ -axis. Indeed, this relationship appears to be stronger than that between  $Q_0$  and  $H$ .

No other prominent first-order interactions of model inputs with  $H$  are apparent, but there is evidence in figure 5 of second-order interactions. While there is no strong first-order dependence of  $H$  on the no-wind entrainment coefficient  $k_s$ , variation in  $k_s$  does have an influence on  $H$  through an interaction with  $k_w$ . In particular, the highest values of  $H$  are achieved when both  $k_w$  and  $k_s$  take values at the lower end of their ranges. Increasing  $k_s$  while leaving  $k_w$  (approximately) fixed results in smaller values of  $H$ .

By including the height at which condensation occurs as a coordinate axis, we are able to examine the control of the model inputs on the phase change of water vapour in the plume and the influence of this on the plume height. Figure 5 shows that there is a threshold on the plume height of approximately 8.2 km below which condensation does not occur for any of the sampled inputs. However, the strong first-order dependence of the plume height on both of the source mass flux  $Q_0$  and the wind entrainment coefficient  $k_w$  means that there is no clear criteria for the source conditions that results in condensation.

It is notable in figure 5 that there are fewer trajectories passing through the upper half of the plume height axis than pass through the lower half of this axis. This indicates a skewed distribution of plume heights (with a relatively long upper tail) even though all model inputs are sampled from uniform distributions. Furthermore, as the relatively high rising plumes are more likely to encounter conditions for which condensation of water vapour can occur, there is evidence that the long upper tail is due to the effects of moisture on the plume dynamics.

In table 2 we report the first-order and total effects sensitivity indices for case (i) where the source mass flux is specified and plume height is calculated. The values of the sensitivity indices confirm the inferences that were drawn from the parallel coordinates visualisation (figure 5), although much larger sampling designs are constructed to compute converged values of the sensitivity indices. The variance in the distribution of plume heights is dominantly due to variation in the wind entrainment coefficient  $k_w$  (i.e. the magnitude of the sensitivity indices corresponding to  $k_w$  are the largest within this set

Table 2: First-order (upper panel) and total effects (lower panel) sensitivity indices for the weak eruption with wind and specified source mass flux. A 95% confidence interval is estimated by a bootstrap of the sampled values.

Parameter (symbol)	First-order sensitivity index	95% Confidence interval
Entrainment coefficient due to wind ( $k_w$ )	$5.9 \times 10^{-1}$	$[5.7 \times 10^{-1}, 5.9 \times 10^{-1}]$
Source mass flux ( $Q_0$ )	$3.5 \times 10^{-1}$	$[3.5 \times 10^{-1}, 3.6 \times 10^{-1}]$
Wind speed scale factor ( $\lambda$ )	$1.8 \times 10^{-2}$	$[1.4 \times 10^{-2}, 1.8 \times 10^{-2}]$
Entrainment coefficient in absence of wind ( $k_s$ )	$1.6 \times 10^{-2}$	$[1.6 \times 10^{-2}, 2.0 \times 10^{-2}]$
Magmatic temperature ( $T_0$ )	$4.5 \times 10^{-3}$	$[3.9 \times 10^{-3}, 5.5 \times 10^{-3}]$
Mass fraction of gas ( $n_0$ )	$2.0 \times 10^{-4}$	$[-5.8 \times 10^{-5}, 2.9 \times 10^{-4}]$
Exit velocity ( $U_0$ )	$6.2 \times 10^{-5}$	$[-1.5 \times 10^{-4}, 4.7 \times 10^{-5}]$
	Total effects sensitivity index	95% Confidence interval
Entrainment coefficient due to wind ( $k_w$ )	$6.1 \times 10^{-1}$	$[6.1 \times 10^{-1}, 6.1 \times 10^{-1}]$
Source mass flux ( $Q_0$ )	$3.7 \times 10^{-1}$	$[3.7 \times 10^{-1}, 3.7 \times 10^{-1}]$
Entrainment coefficient in absence of wind ( $k_s$ )	$2.5 \times 10^{-2}$	$[2.5 \times 10^{-2}, 2.5 \times 10^{-2}]$
Wind speed scale factor ( $\lambda$ )	$1.9 \times 10^{-2}$	$[1.9 \times 10^{-2}, 1.9 \times 10^{-2}]$
Magmatic temperature ( $T_0$ )	$4.7 \times 10^{-3}$	$[4.7 \times 10^{-3}, 4.8 \times 10^{-3}]$
Mass fraction of gas ( $n_0$ )	$2.2 \times 10^{-4}$	$[2.1 \times 10^{-4}, 2.2 \times 10^{-4}]$
Exit velocity ( $U_0$ )	$7.2 \times 10^{-5}$	$[7.1 \times 10^{-5}, 7.2 \times 10^{-5}]$

of model inputs) and, furthermore, this is predominately a first-order dependence since the total effects index does not differ substantially from the first-order index. Therefore, if the wind entrainment coefficient was held fixed, then the variation in the plume height would be greatly reduced. Additionally, we note that the variation of the plume height also has a strong first-order influence on the variance of the source mass flux. The no-wind entrainment coefficient  $k_s$  and the wind-scale factor  $\lambda$  have a smaller influence on the variance of the plume height, and we note that the total effects index corresponding to  $k_s$  is larger than the corresponding first-order index. Therefore, the no-wind entrainment coefficient acts in combination with other model inputs to result in variations in the predicted plume height. The sensitivity indices for the remaining model inputs are of much small magnitude, indicating that variations in these inputs make only a small contribution to the variance in the prediction of the plume height. The skewness of the distribution of the model prediction of the plume heights is not revealed in the sensitivity indices, highlighting the importance of visualisation alongside the calculation of the summary statistics.

In figure 6 we show the parallel coordinates plot when the plume top height is specified and the source mass flux is inferred through an inverse calculation. We observe a strong first-order dependence of the source mass

flux  $Q_0$  on the wind entrainment coefficient  $k_w$ , with relatively high values of the source mass flux when  $k_w$  takes relatively large values (demonstrated by line segments that connected these variable axes that are almost orthogonal to the axes). While the source mass flux is related to the plume height, with typically high plumes resulting in high values of the source mass flux, it is notable that the highest plume height in this sample does not lead to the largest source mass flux as the greatest  $Q_0$  value occurs when of  $k_w \approx 1.0$  (i.e. the greatest value of  $k_w$  in the sample).

Figure 6 also identifies a threshold on the plume height of approximately 8.2 km below which condensation does not occur for any of the sampled inputs. However, exceeding this height does not always result in condensation, as there are two trajectories that exceed the threshold height yet have no condensation (i.e.  $H_c = 0$ ). Tracing these trajectories we find that both have relatively low values for both the volatile mass fraction  $n_0$  and the magmatic temperature  $T_0$ . The height at which condensation occurs does not appear to be strongly related to the predicted value of the source mass flux  $Q_0$ .

The sensitivity indices for case (ii) where the plume height is specified and the source mass flux is determined by inverse modelling are reported in table 3. The magnitude of the indices are similar to those found when the source mass flux is specified (table 2), and therefore the ranking of the model inputs by their influence on the variance of the model output is similar. Note the negative value of the first-order sensitivity index for the exit velocity indicates incomplete convergence of the sampling estimator for this quantity. This slow convergence indicates the low first-order influence of the exit velocity on the inferred source mass flux.

#### 4.2. Weak eruption without wind

When the wind is removed from the inputs to the weak eruption case study, the plume rises vertically and the entrainment is reduced. Therefore, for specified source conditions, the plume reaches higher altitudes than are found in the windy environment. For case (i) the source mass flux is fixed at  $Q_0 = 1.5 \times 10^6$  kg/s and the plume top height is found to be  $H = 9.16$  km above the vent, which is a factor of three greater than the height attained when the wind is included. For case (ii) when the plume top height is fixed at  $H = 6$  km above the vent the source mass flux is found to be  $Q_0 = 1.9 \times 10^5$  kg/s using the reference values for model inputs, a value two orders

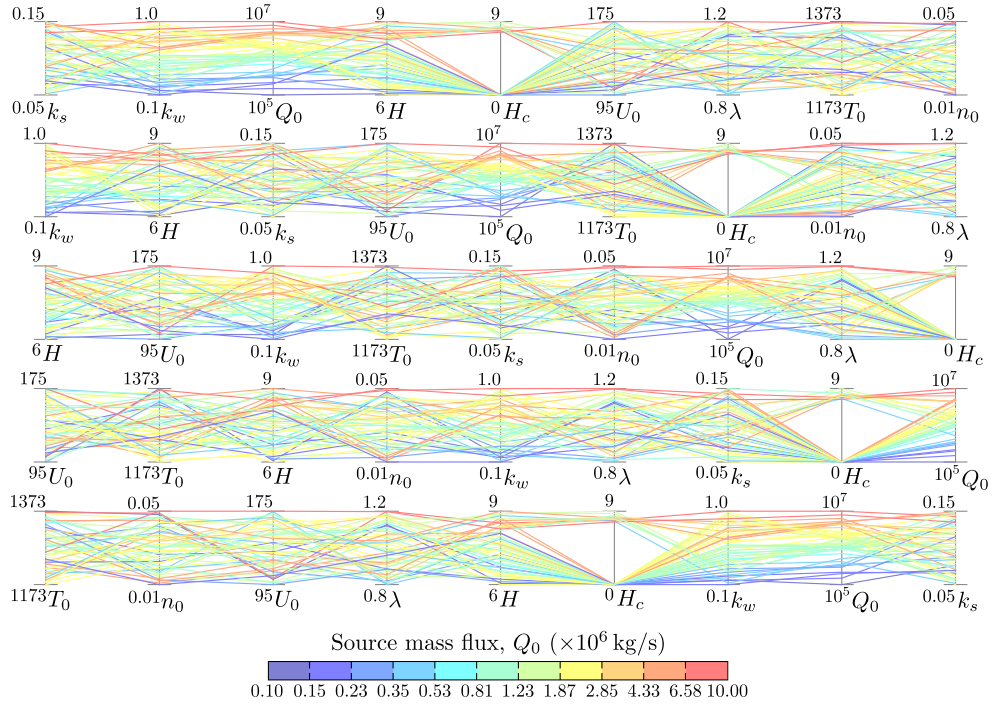


Figure 6: Parallel coordinates plots for the weak eruption case with wind included and the plume height specified. The entrainment coefficients  $k_s$  and  $k_w$ , exit velocity  $U_0$  (measured in m/s), magmatic temperature  $T_0$  (K), volatile mass fraction  $n_0$ , wind speed scale factor  $\lambda$ , and the plume top height  $H$  (km) are varied using a Latin hypercube design with 50 sampling points. The source mass flux  $Q_0$  (kg/s) is determined through an inversion calculation. Note  $Q_0$  is plotted on a logarithmic scale. The height at which condensation occurs in the plume,  $H_c$  (km), is also plotted, with  $H_c = 0$  if no condensation occurs. Trajectories through the coordinate axis represent individual model evaluations, and these are coloured using the inferred source mass flux  $Q_0$ . In each row, the same numerical output is plotted but the ordering of the axes are permuted to aid with the visual interpretation of the sensitivity to input values.

Table 3: First-order (upper panel) and total effects (lower panel) sensitivity indices for the weak eruption with wind and specified plume height. A 95% confidence interval is estimated by a bootstrap of the sampled values.

Parameter (symbol)	First-order sensitivity index	95% Confidence interval
Entrainment coefficient due to wind ( $k_w$ )	$7.0 \times 10^{-1}$	$[6.3 \times 10^{-1}, 9.6 \times 10^{-1}]$
Plume top height ( $H$ )	$2.6 \times 10^{-1}$	$[1.7 \times 10^{-1}, 3.7 \times 10^{-1}]$
Wind speed scale factor ( $\lambda$ )	$1.1 \times 10^{-2}$	$[-1.7 \times 10^{-2}, 4.3 \times 10^{-2}]$
Magmatic temperature ( $T_0$ )	$6.4 \times 10^{-3}$	$[-1.4 \times 10^{-2}, 1.5 \times 10^{-2}]$
Entrainment coefficient in absence of wind ( $k_s$ )	$4.3 \times 10^{-3}$	$[-2.4 \times 10^{-2}, 3.4 \times 10^{-2}]$
Mass fraction of gas ( $n_0$ )	$1.3 \times 10^{-4}$	$[-1.9 \times 10^{-3}, 3.5 \times 10^{-3}]$
Exit velocity ( $U_0$ )	$-1.6 \times 10^{-4}$	$[-2.4 \times 10^{-4}, 1.3 \times 10^{-3}]$
	Total effects sensitivity index	95% Confidence interval
Entrainment coefficient due to wind ( $k_w$ )	$7.0 \times 10^{-1}$	$[6.9 \times 10^{-1}, 7.1 \times 10^{-1}]$
Plume top height ( $H$ )	$2.5 \times 10^{-1}$	$[2.5 \times 10^{-1}, 2.5 \times 10^{-1}]$
Wind speed scale factor ( $\lambda$ )	$2.4 \times 10^{-2}$	$[2.3 \times 10^{-2}, 2.4 \times 10^{-2}]$
Entrainment coefficient in absence of wind ( $k_s$ )	$2.1 \times 10^{-2}$	$[2.1 \times 10^{-1}, 2.2 \times 10^{-2}]$
Magmatic temperature ( $T_0$ )	$5.6 \times 10^{-3}$	$[5.5 \times 10^{-3}, 5.6 \times 10^{-3}]$
Mass fraction of gas ( $n_0$ )	$1.9 \times 10^{-4}$	$[1.9 \times 10^{-4}, 1.9 \times 10^{-4}]$
Exit velocity ( $U_0$ )	$8.8 \times 10^{-5}$	$[8.6 \times 10^{-5}, 8.9 \times 10^{-5}]$

of magnitude smaller than the source mass flux predicted by the model when the wind is included.

Figures 7 and 8 show parallel coordinates plots indicating the model dependencies for case (i) and case (ii), respectively. When the source mass flux is specified (figure 7) the predicted plume height is most sensitive the values taken for the no-wind entrainment coefficient  $k_s$  and the source mass flux  $Q_0$ . Similarly, when the plume height is specified (figure 8) the predicted value of the source mass flux is strongly controlled by the no-wind entrainment coefficient  $k_s$  and the height of the plume  $H$ . The remaining source variables have little influence on the source mass flux determined by the model. The tabulated values of the sensitivity indices in tables 4 and 5 are in support of these inferences.

There is no clear relationship between the height at which condensation occurs in the plume and the plume height when the latter is specified as a model input (figure 8). In contrast, when the source mass flux is specified (figure 7), the height at which condensation occurs is strongly coupled to the plume height (and so the source mass flux), and is also influenced by the value taken for the entrainment coefficient  $k_s$ . This demonstrates that the height at which condensation occurs in the plume is related to the source conditions and the efficiency of mixing of ambient air. Note that in this case,

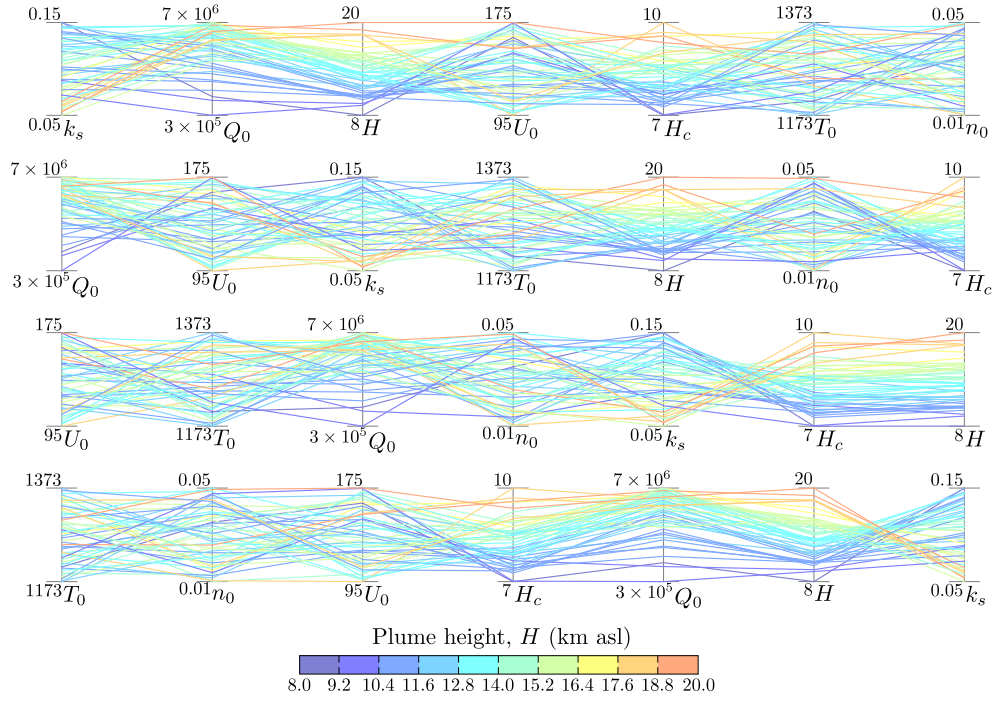


Figure 7: Parallel coordinates plots for the weak eruption case without wind and the source mass flux specified. The no-wind entrainment coefficient  $k_s$ , exit velocity  $U_0$  (m/s), magmatic temperature  $T_0$  (K), volatile mass fraction  $n_0$ , and the source mass flux  $Q_0$  (kg/s) are varied using a Latin hypercube design with 50 sampling points. The plume height  $H$  (km) is calculated. Note  $Q_0$  is plotted on a logarithmic scale. The height at which condensation occurs in the plume,  $H_c$  (km), is also plotted, with  $H_c = 0$  if no condensation occurs. Trajectories through the coordinate axis represent individual model evaluations, and these are coloured using the plume height  $H$ . In each row, the same numerical output is plotted but the ordering of the axes are permuted to aide with the visual interpretation of the sensitivity to input values.

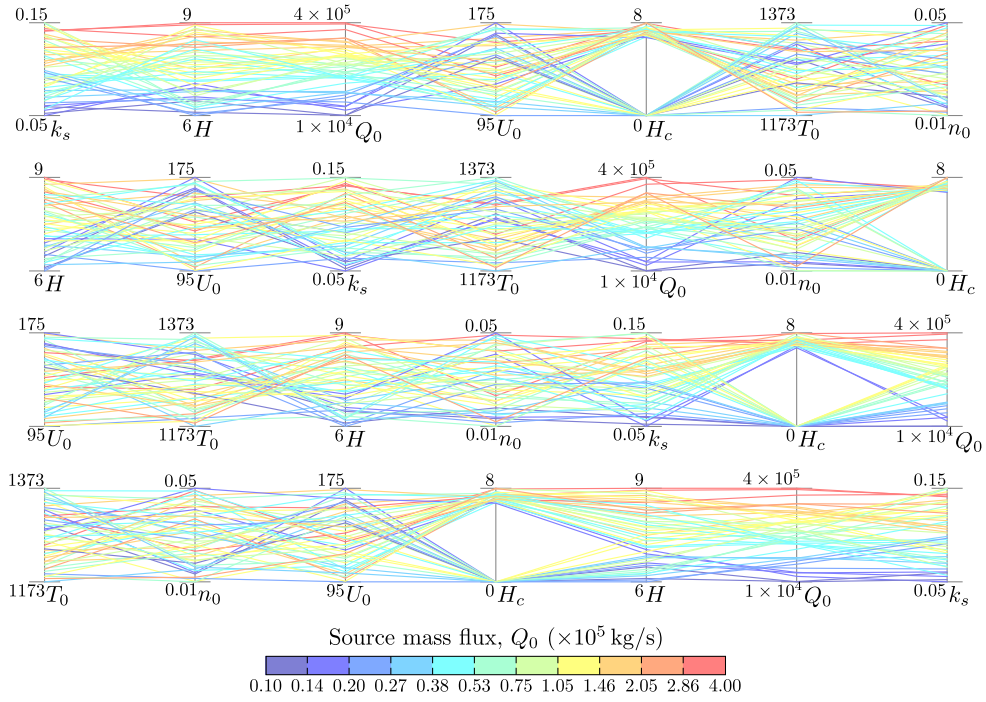


Figure 8: Parallel coordinates plots for the weak eruption case without wind and the plume height specified. The no-wind entrainment coefficient  $k_s$ , exit velocity  $U_0$  (m/s), magmatic temperature  $T_0$  (K), volatile mass fraction  $n_0$ , and the plume top height  $H$  (km) are varied using a Latin hypercube design with 50 sampling points. The source mass flux  $Q_0$  (kg/s) is determined through an inversion calculation. Note  $Q_0$  is plotted on a logarithmic scale. The height at which condensation occurs in the plume,  $H_c$  (km), is also plotted, with  $H_c = 0$  if no condensation occurs. Trajectories through the coordinate axis represent individual model evaluations, and these are coloured using the inferred source mass flux  $Q_0$ . In each row, the same numerical output is plotted but the ordering of the axes are permuted to aide with the visual interpretation of the sensitivity to input values.

Table 4: First-order (upper panel) and total effects (lower panel) sensitivity indices for the weak eruption without wind and specified source mass flux. A 95% confidence interval is estimated by a bootstrap of the sampled values.

Parameter (symbol)	First-order sensitivity index	95% Confidence interval
Source mass flux ( $Q_0$ )	$5.0 \times 10^{-1}$	$[5.0 \times 10^{-1}, 5.1 \times 10^{-1}]$
Entrainment coefficient in absence of wind ( $k_s$ )	$4.6 \times 10^{-1}$	$[4.6 \times 10^{-1}, 4.6 \times 10^0]$
Magmatic temperature ( $T_0$ )	$4.8 \times 10^{-3}$	$[4.8 \times 10^{-3}, 5.2 \times 10^{-3}]$
Exit velocity ( $U_0$ )	$7.7 \times 10^{-4}$	$[7.1 \times 10^{-4}, 8.8 \times 10^{-4}]$
Mass fraction of gas ( $n_0$ )	$5.5 \times 10^{-4}$	$[4.7 \times 10^{-4}, 6.4 \times 10^{-4}]$
	Total effects sensitivity index	95% Confidence interval
Source mass flux ( $Q_0$ )	$5.3 \times 10^{-1}$	$[5.3 \times 10^{-1}, 5.3 \times 10^{-1}]$
Entrainment coefficient in absence of wind ( $k_s$ )	$5.0 \times 10^{-1}$	$[5.0 \times 10^{-1}, 5.1 \times 10^{-1}]$
Magmatic temperature ( $T_0$ )	$5.4 \times 10^{-3}$	$[5.4 \times 10^{-3}, 5.4 \times 10^{-3}]$
Exit velocity ( $U_0$ )	$8.4 \times 10^{-4}$	$[8.4 \times 10^{-4}, 8.4 \times 10^{-4}]$
Mass fraction of gas ( $n_0$ )	$8.4 \times 10^{-4}$	$[8.4 \times 10^{-4}, 8.4 \times 10^{-4}]$

Table 5: First-order (upper panel) and total effects (lower panel) sensitivity indices for the weak eruption without wind and specified plume height. A 95% confidence interval is estimated by a bootstrap of the sampled values.

Parameter (symbol)	First-order sensitivity index	95% Confidence interval
Entrainment coefficient in absence of wind ( $k_s$ )	$4.9 \times 10^{-1}$	$[2.4 \times 10^{-1}, 1.1 \times 10^0]$
Plume top height ( $H$ )	$4.7 \times 10^{-1}$	$[1.7 \times 10^{-2}, 8.8 \times 10^{-1}]$
Magmatic temperature ( $T_0$ )	$3.8 \times 10^{-3}$	$[-2.5 \times 10^{-2}, 8.1 \times 10^{-2}]$
Mass fraction of gas ( $n_0$ )	$3.6 \times 10^{-4}$	$[-7.3 \times 10^{-3}, 1.7 \times 10^{-2}]$
Exit velocity ( $U_0$ )	$-2.8 \times 10^{-4}$	$[-5.7 \times 10^{-3}, 1.8 \times 10^{-2}]$
	Total effects sensitivity index	95% Confidence interval
Entrainment coefficient in absence of wind ( $k_s$ )	$5.1 \times 10^{-1}$	$[4.9 \times 10^{-1}, 5.3 \times 10^{-1}]$
Plume top height ( $H$ )	$4.9 \times 10^{-1}$	$[4.7 \times 10^{-1}, 5.0 \times 10^{-1}]$
Magmatic temperature ( $T_0$ )	$7.7 \times 10^{-3}$	$[7.5 \times 10^{-3}, 8.1 \times 10^{-3}]$
Exit velocity ( $U_0$ )	$4.0 \times 10^{-4}$	$[3.8 \times 10^{-4}, 4.1 \times 10^{-4}]$
Mass fraction of gas ( $n_0$ )	$3.8 \times 10^{-4}$	$[3.6 \times 10^{-4}, 3.9 \times 10^{-4}]$

condensation is predicted to occur in the plume for all of the conditions in this sample.

#### 4.3. Strong eruption with wind

We consider next the strong eruption scenario with the atmospheric wind included in the atmospheric profiles. The PlumeRise model results using the specified ‘reference’ model inputs are shown in figure 9. For case (i) the source mass flux is fixed at  $Q_0 = 1.5 \times 10^9$  kg/s and the plume top height is found to be  $H = 35.7$  km above the vent which is 1.5 km asl. For case (ii) the plume top height is fixed at  $H = 37$  km above the vent and the source mass flux is found to be  $Q_0 = 1.8 \times 10^9$  kg/s using the reference values for model inputs.

A parallel coordinates plot for a sample of 50 sets of model inputs is shown in figure 10 for case (i) where the source mass flux is specified. In contrast to the weak eruption scenarios, we find that the column collapse can occur in this setting. Model input sets that lead to column collapse are identified as dashed lines segments in figure 10.

Figure 10 shows that, for those input sets that produce buoyant plumes, the plume heights are predicted to be high in the stratosphere, and the value predicted for  $H$  is strongly controlled by the source mass flux  $Q_0$ , with higher plumes for larger values of the source mass flux, and weakly by the entrainment coefficients  $k_s$  and  $k_w$ , with the highest plumes occurring when both entrainment parameters take low values. There is evidence that the source temperature has an influence on the plume height, typically with higher source temperatures leading to greater plume heights, although the dependence on  $T_0$  is weaker than for  $Q_0$ ,  $k_s$  and  $k_w$  as indicated by the input set with the highest source temperature which produces the lowest buoyant plume for this sample set. The remaining model inputs do not strongly influence the calculated values of the plume heights for conditions where the plume becomes buoyant.

Column collapse is found to occur for relatively high values of the source mass flux (figure 10). When collapse occurs, the exit velocity  $U_0$  (most strongly), gas mass fraction  $n_0$  and magmatic temperature (least strongly) determine the collapse conditions. This is consistent with the values of the total sensitivity indices in table 6. However, the occurrence of column collapse results in a strongly bi-modal distribution of the calculated plume heights (as seen in figure 10), so the use of variance-based sensitivity indices can be misleading. Furthermore, convergence of the indices requires substantially

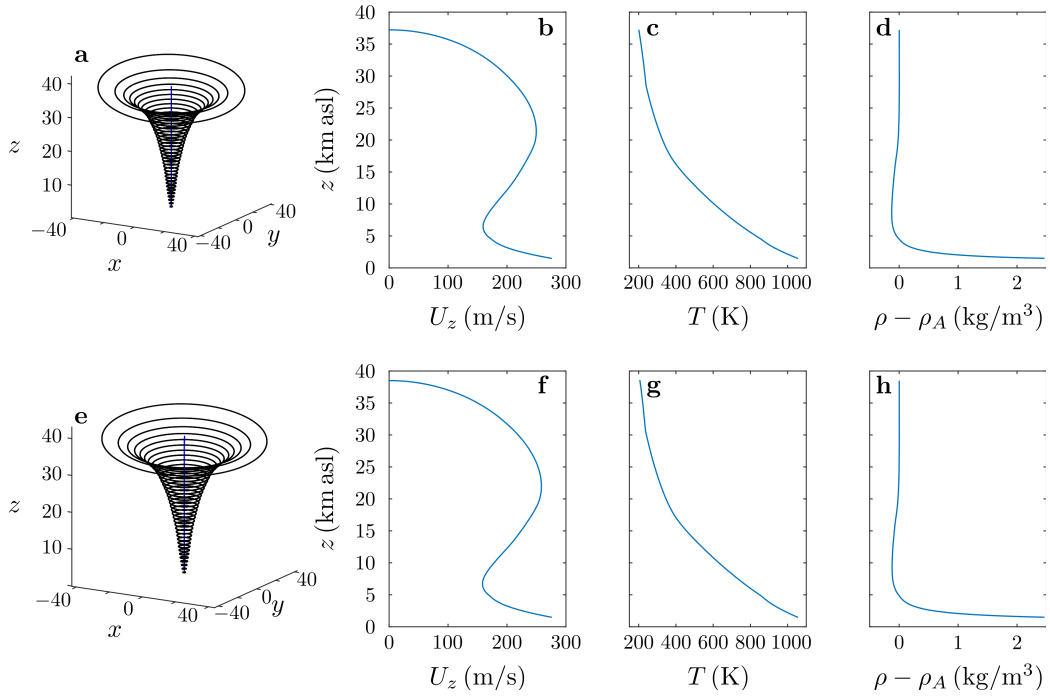


Figure 9: Solutions of the PlumeRise model with the reference input values for the strong eruption scenario. The vent is specified to be at an altitude of 1.5 km asl. In **a–d** the source mass flux is set at  $Q_0 = 1.5 \times 10^9$  kg/s (case i). In **e–h** the plume height is specified to be  $H = 38.5$  km asl (case ii). **a** and **e** illustrate the plume trajectory and radius. The vertical velocity (**b** and **f**), plume temperature (**c** and **g**), and the density difference between the plume and atmosphere (**d** and **h**) as functions of the height are shown.

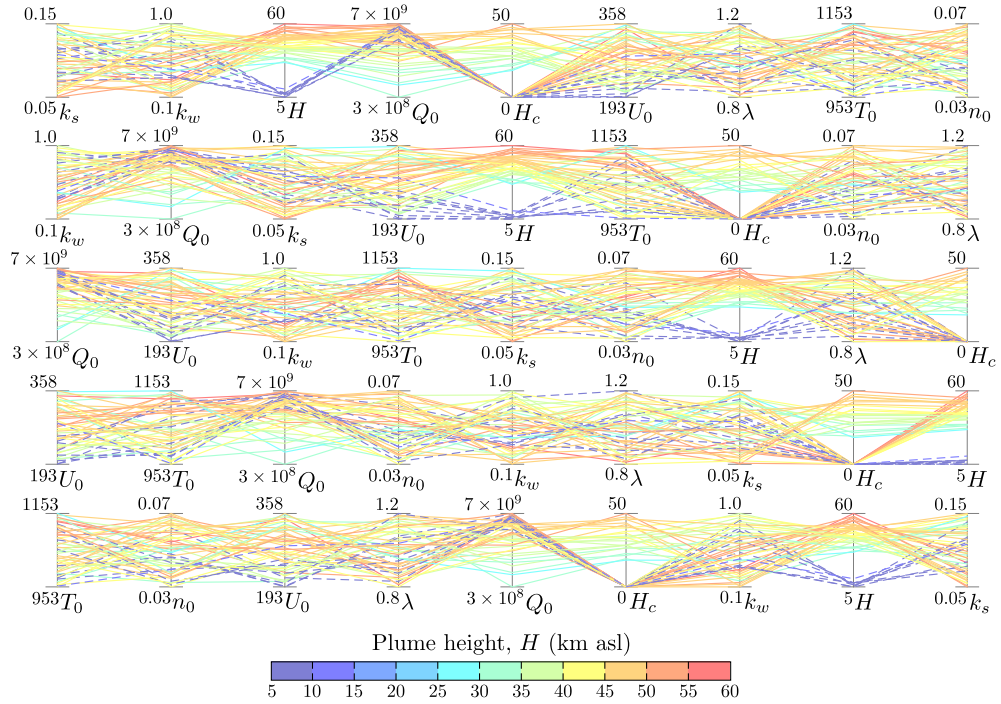


Figure 10: Parallel coordinates plots for the strong eruption case with wind included and the source mass flux specified. The entrainment coefficients  $k_s$  and  $k_w$ , exit velocity  $U_0$  (measured in m/s), magmatic temperature  $T_0$  (K), volatile mass fraction  $n_0$ , wind speed scale factor  $\lambda$ , and the source mass flux  $Q_0$  (kg/s) are varied using a Latin hypercube design with 50 sampling points. The plume height  $H$  (km) is determined. Note  $Q_0$  is plotted on a logarithmic scale. The height at which condensation occurs in the plume,  $H_c$  (km), is also plotted, with  $H_c = 0$  if no condensation occurs. Trajectories through the coordinate axis represent individual model evaluations, and these are coloured using the inferred source mass flux  $Q_0$ . Dashed line segments indicate a model input set that leads to column collapse. In each row, the same numerical output is plotted but the ordering of the axes are permuted to aide with the visual interpretation of the sensitivity to input values.

Table 6: First-order (upper panel) and total effects (lower panel) sensitivity indices for the strong eruption with wind and specified source mass flux. A 95% confidence interval is estimated by a bootstrap of the sampled values.

Parameter (symbol)	First-order sensitivity index	95% Confidence interval
Exit velocity ( $U_0$ )	$2.9 \times 10^{-1}$	$[2.9 \times 10^{-1}, 3.0 \times 10^{-1}]$
Magmatic temperature ( $T_0$ )	$7.5 \times 10^{-2}$	$[7.0 \times 10^{-2}, 8.2 \times 10^{-2}]$
Mass fraction of gas ( $n_0$ )	$5.8 \times 10^{-2}$	$[5.3 \times 10^{-2}, 6.6 \times 10^{-2}]$
Entrainment coefficient in absence of wind ( $k_s$ )	$1.3 \times 10^{-2}$	$[1.2 \times 10^{-2}, 1.5 \times 10^{-2}]$
Wind speed scale factor ( $\lambda$ )	$-1.1 \times 10^{-3}$	$[-3.2 \times 10^{-3}, 7.9 \times 10^{-4}]$
Source mass flux ( $Q_0$ )	$-1.3 \times 10^{-3}$	$[-8.0 \times 10^{-3}, 6.3 \times 10^{-3}]$
Entrainment coefficient due to wind ( $k_w$ )	$-5.1 \times 10^{-3}$	$[-8.9 \times 10^{-3}, -2.8 \times 10^{-4}]$
	Total effects sensitivity index	95% Confidence interval
Exit velocity ( $U_0$ )	$7.7 \times 10^{-1}$	$[7.6 \times 10^{-1}, 7.7 \times 10^{-1}]$
Source mass flux ( $Q_0$ )	$4.1 \times 10^{-1}$	$[4.1 \times 10^{-1}, 4.1 \times 10^{-1}]$
Mass fraction of gas ( $n_0$ )	$3.6 \times 10^{-1}$	$[3.5 \times 10^{-1}, 3.6 \times 10^{-1}]$
Magmatic temperature ( $T_0$ )	$2.9 \times 10^{-1}$	$[2.8 \times 10^{-1}, 2.9 \times 10^{-1}]$
Entrainment coefficient due to wind ( $k_w$ )	$1.5 \times 10^{-1}$	$[1.5 \times 10^{-1}, 1.6 \times 10^{-1}]$
Wind speed scale factor ( $\lambda$ )	$3.4 \times 10^{-2}$	$[3.3 \times 10^{-2}, 3.5 \times 10^{-2}]$
Entrainment coefficient in absence of wind ( $k_s$ )	$2.2 \times 10^{-2}$	$[2.2 \times 10^{-2}, 2.3 \times 10^{-2}]$

larger samples. For example, the indices reported in table 6 are calculated from a sample of 100000 model input sets and the first-order indices corresponding to  $k_w$ ,  $Q_0$  and  $\lambda$  have not yet converged (as negative values are found). Therefore, the visualisation in figure 10 together with the sensitivity indices in table 6 is needed to gain insight into the model sensitivities.

A parallel coordinates plot for case (ii) where the plume height is specified as a model input and the source mass flux is predicted through a model inversion is shown in figure 11. For the strong eruption case the model inversion can fail to find solutions due to column collapse, where the erupted material does not become buoyant. Model input sets that lead to failure of the inversion calculation are identified as grey dashed lines segments in figure 11. Note we plot points for the source mass flux in these cases in order to avoid breaking the line segments on the parallel coordinates plots. The failure of the inversion calculation means that the sensitivity indices associated with the determination of the source mass flux from a specified plume height cannot be calculated in this case. However, the visualisation allows us to assess the sensitivity to variations in the model inputs.

The predicted source mass flux is strongly related to the specified height of the plume (figure 11), with higher values of  $Q_0$  when the plume top height is large. The no-wind entrainment coefficient  $k_s$  has relatively more influence

on the predicted source mass flux than the wind entrainment coefficient  $k_w$ , in contrast to the weak eruption case. The source mass flux is predicted to take large values when  $k_s$  has values towards the upper end of its range, but there is evidence of a second-order interaction between  $k_s$  and  $k_w$  (e.g. low values of one of these parameters can be compensated by high values of the other). There is a weak dependence of the source mass flux on the value of the source temperature, typically with larger values of  $Q_0$  when  $T_0$  has relatively low values. There is no clear systematic influence of the other model inputs on the predicted source mass flux when the plume becomes buoyant.

From the few model input sets shown in figure 11 that lead to failure of the inversion calculation, and inspection of similar plots for larger sample sizes (figure 12), the influence of the source conditions on column collapse can be examined. Figures 11 and 12 show that the value taken for the exit velocity  $U_0$  strongly determines column collapse, with low values of  $U_0$  leading to eruption columns that do not become buoyant. Relatively high values of the exit velocity only result in collapse if either or both of the entrainment coefficients take relatively high values. Furthermore, relatively low values of both the magmatic temperature  $T_0$  and source gas mass fraction  $n_0$  are found for those plumes that collapse. The values of the temperature and exit velocity are also linked, with relatively high exit velocities only resulting in collapse if the temperature is low and *vice versa*.

#### 4.4. Strong eruption without wind

We now consider the strong eruption with the atmospheric wind removed from the model forcing. A parallel coordinates plot for a sample of 50 model input sets for case (i), when the source mass flux is specified and the plume height is calculated is shown in figure 13. The strong dependence of the plume height  $H$  on the source mass flux  $Q_0$  is again observed for input sets that result in buoyant plumes. The no-wind entrainment coefficient  $k_s$  also has a strong control, with the plume height predicted to be higher when  $k_s$  has relatively low values. There is some evidence in figure 13 that the magmatic temperature  $T_0$  influences the plume height, with higher plumes occurring when the source is relatively hot. Interestingly, the model predicts that a substantial proportion of the high rising plumes do not have condensation during the ascent.

Column collapse is predicted to occur for 14 of the 50 model input sets (denote by dashed lines in figure 13). These collapsing conditions include a

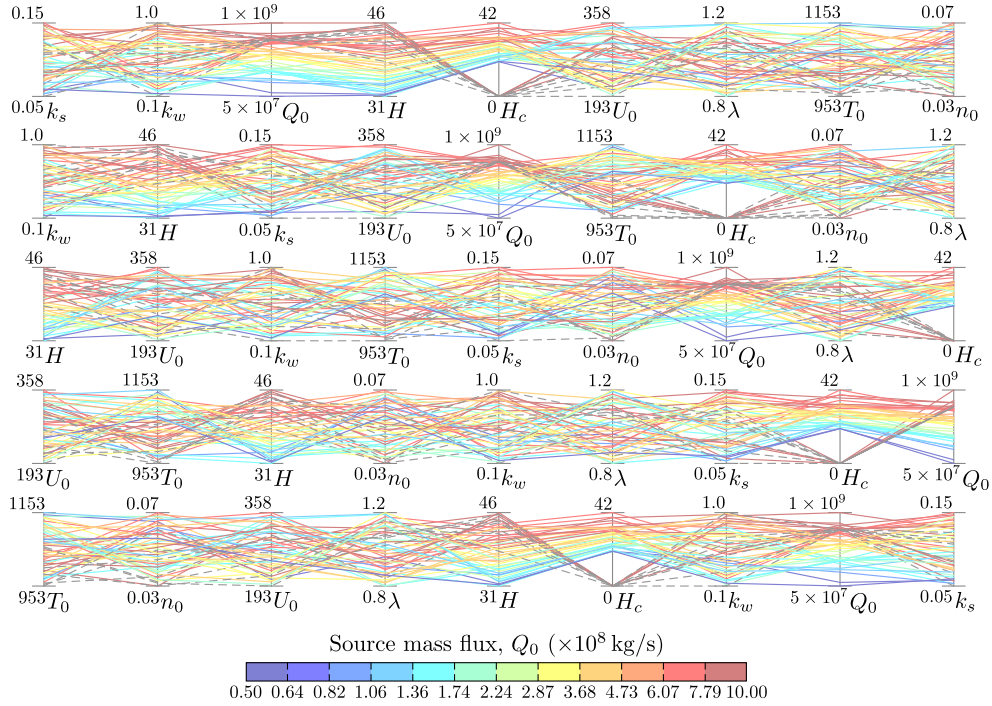


Figure 11: Parallel coordinates plot for the strong eruption case with wind included and the plume height specified. The entrainment coefficients  $k_s$  and  $k_w$ , exit velocity  $U_0$  (measured in m/s), magmatic temperature  $T_0$  (K), volatile mass fraction  $n_0$ , wind speed scale factor  $\lambda$ , and the plume top height  $H$  (km) are varied using a Latin hypercube design with 50 sampling points. The source mass flux  $Q_0$  (kg/s) is determined through an inversion calculation. Note  $Q_0$  is plotted on a logarithmic scale. The height at which condensation occurs in the plume,  $H_c$  (km), is also plotted, with  $H_c = 0$  if no condensation occurs. Trajectories through the coordinate axis represent individual model evaluations, and these are coloured using the inferred source mass flux  $Q_0$ . Grey dashed line segments indicate a input set where the inversion calculation failed, so the target height could not be attained. In each row, the same numerical output is plotted but the ordering of the axes are permuted to aide with the visual interpretation of the sensitivity to input values.

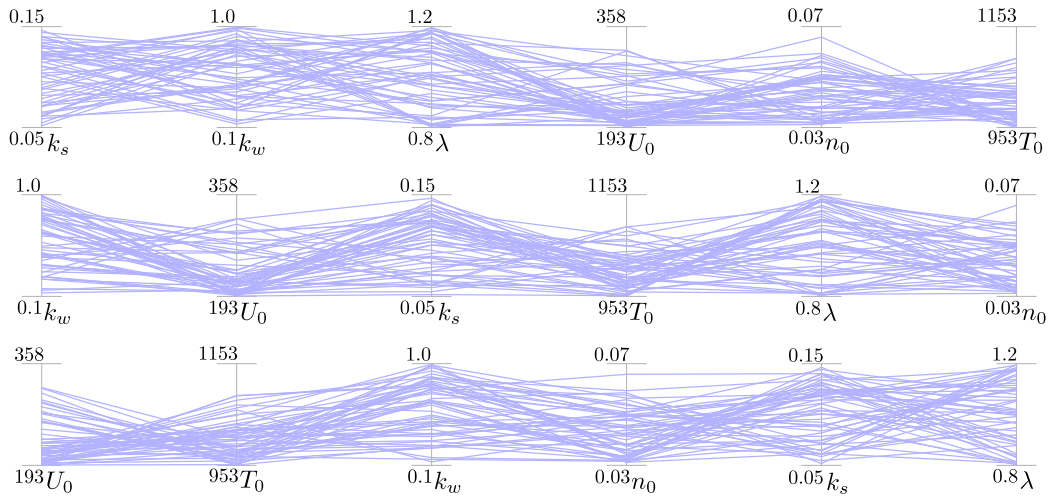


Figure 12: A parallel coordinates plot of model inputs leading to column collapse for the strong eruption case with wind included and the plume height specified. The entrainment coefficients  $k_s$  and  $k_w$ , exit velocity  $U_0$  (measured in m/s), magmatic temperature  $T_0$  (K), volatile mass fraction  $n_0$ , wind speed scale factor  $\lambda$ , and the plume top height  $H$  (km) are varied using a Latin hypercube design with 500 sampling points. In this sample, 54 input sets result in column collapse and the values of  $k_s$ ,  $k_w$ ,  $U_0$ ,  $T_0$ ,  $n_0$  and  $\lambda$  in these input sets are plotted on parallel coordinate axes and connected by line segments. In each row, the same numerical output is plotted but the ordering of the axes are permuted to aide with the visual interpretation of the sensitivity to input values.

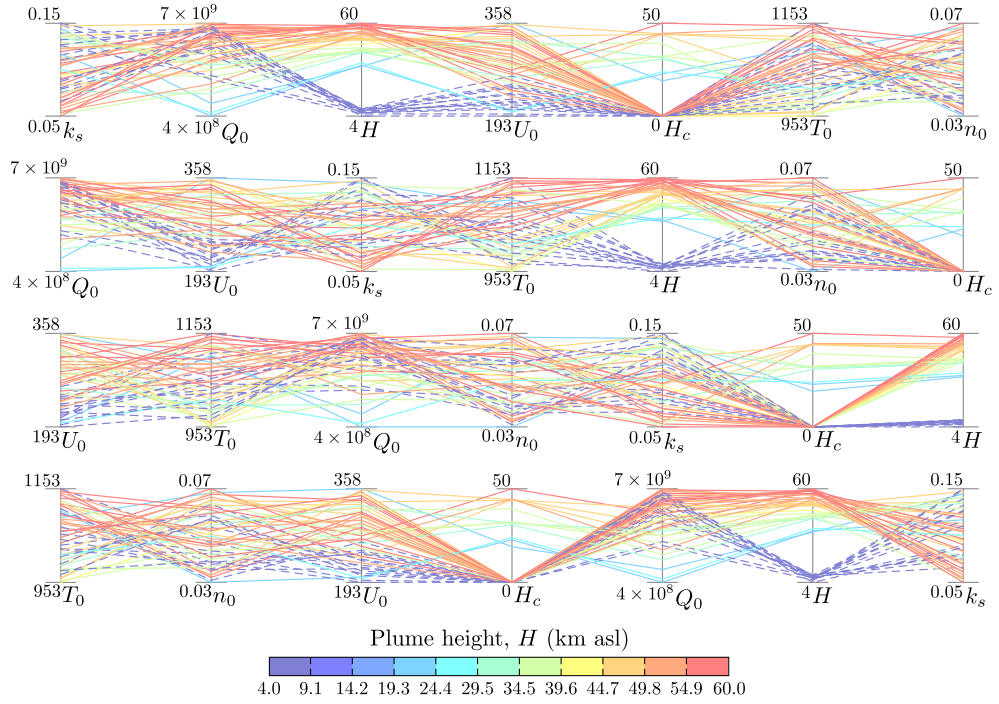


Figure 13: Parallel coordinates plots for the strong eruption case without wind and the source mass flux specified. The no-wind entrainment coefficient  $k_s$ , exit velocity  $U_0$  (measured in m/s), magmatic temperature  $T_0$  (K), volatile mass fraction  $n_0$ , and the source mass flux  $Q_0$  (kg/s) are varied using a Latin hypercube design with 50 sampling points. The plume height  $H$  (km) is determined. Note  $Q_0$  is plotted on a logarithmic scale. The height at which condensation occurs in the plume,  $H_c$  (km), is also plotted, with  $H_c = 0$  if no condensation occurs. Trajectories through the coordinate axis represent individual model evaluations, and these are coloured using the calculated plume height  $H$ . Dashed line segments indicate a model input set that leads to column collapse. In each row, the same numerical output is plotted but the ordering of the axes are permuted to aid with the visual interpretation of the sensitivity to input values.

Table 7: First-order (upper panel) and total effects (lower panel) sensitivity indices for the strong eruption without wind and specified source mass flux. A 95% confidence interval is estimated by a bootstrap of the sampled values.

Parameter (symbol)	First-order sensitivity index	95% Confidence interval
Exit velocity ( $U_0$ )	$4.3 \times 10^{-1}$	$[4.3 \times 10^{-1}, 4.4 \times 10^{-1}]$
Magmatic temperature ( $T_0$ )	$7.3 \times 10^{-2}$	$[7.3 \times 10^{-2}, 7.6 \times 10^{-2}]$
Mass fraction of gas ( $n_0$ )	$6.6 \times 10^{-2}$	$[6.5 \times 10^{-2}, 6.8 \times 10^{-2}]$
Source mass flux ( $Q_0$ )	$2.0 \times 10^{-2}$	$[2.0 \times 10^{-2}, 2.3 \times 10^{-2}]$
Entrainment coefficient in absence of wind ( $k_s$ )	$7.2 \times 10^{-3}$	$[7.0 \times 10^{-3}, 7.7 \times 10^{-3}]$
	Total effects sensitivity index	95% Confidence interval
Exit velocity ( $U_0$ )	$8.0 \times 10^{-1}$	$[8.0 \times 10^{-1}, 8.0 \times 10^{-1}]$
Source mass flux ( $Q_0$ )	$3.5 \times 10^{-1}$	$[3.5 \times 10^{-1}, 3.5 \times 10^{-1}]$
Mass fraction of gas ( $n_0$ )	$2.9 \times 10^{-1}$	$[2.9 \times 10^{-1}, 3.0 \times 10^{-1}]$
Magmatic temperature ( $T_0$ )	$2.4 \times 10^{-1}$	$[2.4 \times 10^{-1}, 2.4 \times 10^{-1}]$
Entrainment coefficient in absence of wind ( $k_s$ )	$1.6 \times 10^{-2}$	$[1.6 \times 10^{-2}, 1.6 \times 10^{-2}]$

larger range of the source mass flux  $Q_0$  than is found when the atmospheric wind is included (see figure 10). Column collapse is typically found when the exit velocity  $U_0$  is relatively low.

The sensitivity indices for case (i) of the strong plume example without wind included are reported in table 7. As the distribution of the predicted plume height is strongly bi-modal, the variance-based sensitivity indices do not comprehensively reveal the model dependencies for this case, and are slowly converging; in table 7 the indices are calculated from a sample of one million model inputs. The sensitivity indices give particular prominence to the exit velocity, indicating the importance of  $U_0$  in determining whether the column becomes buoyant.

A parallel coordinates plot for case (ii) where the plume height is specified and the source mass flux determined, is shown in figure 14 and illustrates the strong relationship between the plume height  $H$  and source mass flux  $Q_0$ . There is also a strong dependence of the predicted value of the source mass flux on the no-wind entrainment coefficient  $k_s$ . In contrast to the strong eruption with wind included, condensation is predicted to occur for all input sets that result in buoyant plumes. Three of the 50 model input sets lead to a failure of the inversion calculation, denoted by dashed grey lines on the figure, and so we do not compute the corresponding sensitivity indices.

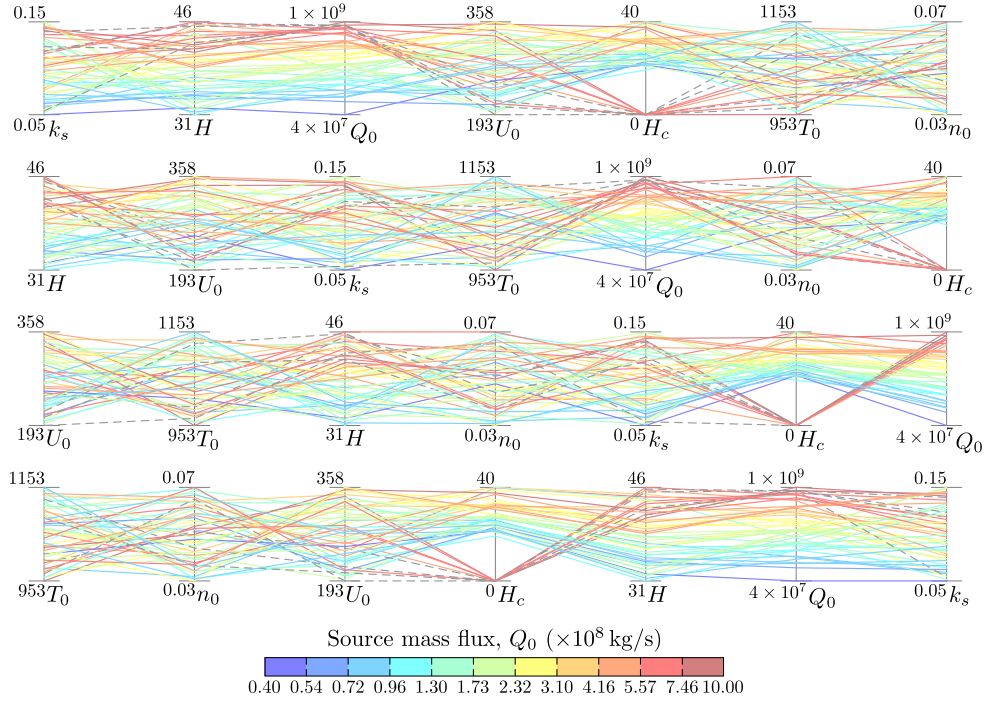


Figure 14: Parallel coordinates plot for the strong eruption case without wind and the plume height specified. The no-wind entrainment coefficient  $k_s$ , exit velocity  $U_0$  (measured in m/s), magmatic temperature  $T_0$  (K), volatile mass fraction  $n_0$ , and the plume top height  $H$  (km) are varied using a Latin hypercube design with 50 sampling points. The source mass flux  $Q_0$  (kg/s) is determined through an inversion calculation. Note  $Q_0$  is plotted on a logarithmic scale. The height at which condensation occurs in the plume,  $H_c$  (km), is also plotted, with  $H_c = 0$  if no condensation occurs. Trajectories through the coordinate axis represent individual model evaluations, and these are coloured using the inferred source mass flux  $Q_0$ . Grey dashed line segments indicate a input set where the inversion calculation failed, so the target height could not be attained. In each row, the same numerical output is plotted but the ordering of the axes are permuted to aide with the visual interpretation of the sensitivity to input values.

## 5. Discussion

The global sensitivity analysis for each of the scenarios considered demonstrates the importance of a relatively small set of the inputs to the model on the predictions. Variations in the source mass flux  $Q_0$  and the entrainment coefficients  $k_s$  and  $k_w$  have the dominant control on the plume height when forward model calculations are performed in the considered ranges for the input parameters. If inverse model calculations are performed, with the plume height specified, then variations in the plume height  $H$  and  $k_s$  and  $k_w$  are dominant in controlling the prediction of the source mass flux. The other inputs have less influence on the model predictions.

As the PlumeRise model is a coupled nonlinear system of equations, it is difficult to anticipate these sensitivities directly from the model formulation. However, for buoyant plumes of a single phase of incompressible fluid that issues from a point source into a linearly stratified quiescent ambient, dimensional analysis suggests a fundamental relationship between the height of the plume, denoted by  $h$  for this idealised setting, and the source buoyancy flux,  $F_0$ , with

$$h = cN^{-3/4}F_0^{1/4} \quad (20)$$

where  $N$  is the buoyancy frequency of the atmosphere defined by

$$N^2 = -\frac{g}{\rho_0} \frac{d\rho_A}{dz}, \quad (21)$$

is assumed to be a positive constant, and  $c$  is a dimensionless constant (Morton et al., 1956). This relationship has been used to motivate the formulation of scaling relationships for volcanic plumes. Sparks et al. (1997) and Mastin et al. (2009) impose a relationship  $H = \alpha Q^\beta$  and use observational data to calibrate the dimensional prefactor  $\alpha$  and the exponent  $\beta$ , and both studies find  $\beta \approx 0.25$ . Other studies (see e.g. Wilson et al., 1978; Settle, 1978; Woods, 1988; Sparks et al., 1997; Degruyter and Bonadonna, 2012) have incorporated the atmospheric buoyancy frequency and used source and atmospheric thermodynamic parameters to express the source buoyancy flux in terms of the source mass flux. Here we use the expression given in Degruyter and Bonadonna (2012) and Woodhouse et al. (2013) as an estimate of the height of a volcanic plume in a quiescent atmosphere,  $H_0$ , with

$$H_0 \approx \frac{0.0013}{\sqrt{k_s}} \left( \frac{g(C_{p0}T_0 - C_A T_{A0})}{\rho_{A0} C_A T_{A0}} \right)^{1/4} N^{-3/4} Q^{1/4}, \quad (22)$$

for  $H_0$  measured in km. Note that for volcanic plumes, the compressibility of the atmosphere is important (as plumes typically rise to heights comparable with the scale height of the atmosphere), and therefore the buoyancy frequency should be calculated using the potential temperature of the atmosphere (Gill, 1982).

For plumes rising in a wind field, the plume height is significantly reduced compared to an equivalent plume rising in quiescent atmosphere. Degruyter and Bonadonna (2012) and Woodhouse et al. (2013) have proposed modifications of the algebraic relationship (22) to explicitly account for the atmospheric wind. The relationships proposed by Degruyter and Bonadonna (2012) and Woodhouse et al. (2013) each have the form,

$$Q_0 = \frac{2^{5/2}\pi k_s^2}{z_1^4} \left[ \frac{\rho_{A0} C_A T_{A0}}{g((C_v n_0 + C_s(1 - n_0))T_0 - C_A T_{A0})} \right] N^3 H^4 f(\mathcal{W}), \quad (23)$$

where  $z_1$  is a calibration parameter (Morton et al., 1956 give  $z_1 = 2.8$  from numerical solutions of an integral model of pure plumes, i.e. with boundary conditions corresponding to a point source of buoyancy with no flux of mass or momentum, while Woodhouse et al. 2013 take  $z_1 = 2.67$  from numerical solutions of an integral model of volcanic plumes in a quiescent Standard Atmosphere). Note, here we have inverted the expression presented in Woodhouse et al. (2013) to give the source mass flux as a function of the plume height. The effect of wind is described by the function  $f(\mathcal{W})$  which is a monotonic increasing function of a dimensionless measure of the wind speed  $\mathcal{W}$ . The models differ in the specification of the dimensionless wind speed  $\mathcal{W}$ , and the form of the function  $f$ . Degruyter and Bonadonna (2012) propose

$$f(\mathcal{W}) = 1 + \frac{z_1^4}{2^{5/2}} \cdot \frac{k_w^2}{6k_s^2} \mathcal{W}, \quad \text{with} \quad \mathcal{W} = \frac{\bar{v}}{\bar{N}H}, \quad (24)$$

while Woodhouse et al. (2013) suggest

$$f(\mathcal{W}) = \left( \frac{1 + b\mathcal{W} + c\mathcal{W}^2}{1 + a\mathcal{W}} \right)^4, \quad \text{with} \quad \mathcal{W} = 1.44 \frac{\dot{\gamma}}{\bar{N}}. \quad (25)$$

Here  $\bar{v}$  and  $\bar{N}$  are the wind speed and buoyancy frequency averaged over the plume height (Degruyter and Bonadonna, 2012),  $\dot{\gamma}$  is representative of the shear rate of the atmospheric wind, and  $a = 0.87 + 0.05k_w/k_s$ ,  $b = 1.09 + 0.32k_w/k_s$  and  $c = 0.06 + 0.03k_w/k_s$  (Woodhouse et al., 2013). The

functional form (24) is obtained by Degruyter and Bonadonna (2012) from a linear combination, with equal weights, of the plume rise height relationship of Morton et al. (1956) for plumes in a quiescent ambient (when  $\mathcal{W} \equiv 0$ ) and the asymptotic expression of Hewett et al. (1971) for the rise height of a pure plume in a uniform cross wind that is appropriate for  $\mathcal{W} \gg 1$  (Hewett et al., 1971). In contrast, the more complex functional form in (25) emerges as Woodhouse et al. (2013) fit an algebraic expression for the plume height as a function of the source mass flux (i.e. the inverse of the expression 23) to numerical solutions of the integral plume model in a standard atmosphere over a range of values of  $\mathcal{W} < 5$  that is typical of wind-blown volcanic plumes rather than employing a combination of the relationships appropriate in the asymptotic regimes  $\mathcal{W} \ll 1$  and  $\mathcal{W} \gg 1$ . However, the physics captured by the algebraic relationships of Degruyter and Bonadonna (2012) and Woodhouse et al. (2013) are essentially identical; the rise height of the plume decreases as the shear rate of the wind increases for a fixed source mass flux, due to enhanced mixing.

The algebraic relationships are simplified descriptions of the dynamics of eruption columns; they can be considered as surrogates of the nonlinear system of ordinary differential equations (in Costa et al. 2016 these relationships are described as 0<sup>th</sup>-degree models). The use of source parameters and representative atmospheric parameters means that these algebraic relationships do not capture the complexity of behaviour found when solving the system of differential equations. For examples, the effects of different stratification in the troposphere and stratosphere (Woods, 1988; Glaze and Baloga, 1996), change of phase of water vapour (Woods, 1993; Glaze et al., 1997; Woodhouse et al., 2013), and local variations in the wind speed with height (Bursik, 2001; Bursik et al., 2009), cannot be explored with the algebraic relationships. Nonetheless, they do provide insight into the sensitivity of the plume height to variations in source conditions.

It is apparent from equation (23) that, when inferring the source mass flux using the model, there is a strong dependence on variations in the plume height. If only the plume height is varied, with all parameters held fixed, then we find from (23) that the change in the source mass flux,  $\delta Q$ , is given by

$$\delta Q = \left[ \left( 1 + \frac{\delta H}{H} \right)^4 - 1 \right] Q_0, \quad (26)$$

where  $Q_0$  is the source mass flux found when the plume rises to height  $H$ ,

Table 8: The change in the source mass flux  $Q_0$  (measured in kg/s) inferred from the plume height when the specified height  $H_0$  (km asl) is changed by  $\pm 20\%$  for each of the eruption scenarios. The other model inputs are held fixed at their reference values.

Eruption scenario	$H_0$	$Q_0$ for $H = H_0$	$Q_0$ for $H = 0.8H_0$ (% change)	$Q_0$ for $H = 1.2H_0$ (% change)
Weak eruption with wind	7.5	$1.08 \times 10^7$	$4.89 \times 10^6$ (-55%)	$2.69 \times 10^7$ (+149%)
Weak eruption without wind	7.5	$1.94 \times 10^5$	$7.00 \times 10^4$ (-64%)	$5.47 \times 10^5$ (+182%)
Strong eruption with wind	38.5	$1.81 \times 10^9$	$6.00 \times 10^8$ (-67%)	$4.93 \times 10^9$ (+172%)
Strong eruption without wind	38.5	$8.71 \times 10^8$	$2.68 \times 10^8$ (-69%)	$2.32 \times 10^9$ (+166%)

and  $\delta H$  is the change in the plume height. Therefore, when the heights are increased by 20% the source mass flux would be expected to increase by a factor of 2, whereas a decrease of the height by 20% would be expected reduce the source mass flux by a factor 0.4. However, these estimates assume that the atmospheric conditions, quantified in (23) by the representative values of the buoyancy frequency  $N$  and the wind strength parameter  $\mathcal{W}$ , do not change when the height is varied. However, the atmospheric structure may be such that relatively small changes in the plume height result in substantial changes to the representative (e.g. column averaged) buoyancy frequency (e.g. if the change in height takes the plume into the stratosphere) or the representative shear rate of the atmospheric wind (e.g. if the change in height results in the plume rising into a region with a locally high wind speed such as jet streams). Table 8 reports the change in the source mass flux inferred by inversion when the plume height alone is changed by  $\pm 20\%$  for each of the scenarios studied, and indicates that the algebraic approximation (26) gives an under-estimate of the change in the source mass flux when there is a variation in the plume height. This demonstrates the importance of dynamical processes occurring above the vent that are not explicitly included in the algebraic relationships.

In a weak wind field (such as that used for the strong eruption case study), the wind parameter  $\mathcal{W}$  is small and  $f(\mathcal{W}) \approx 1$ , so the predicted source mass flux depends on the no-wind entrainment coefficient  $k_s$ , but only weakly on the wind entrainment coefficient  $k_w$ . In contrast, in a strong wind field (such as that used for the weak eruption case study),  $\mathcal{W} > 0$ , and a dependence of the source mass flux on the wind entrainment coefficient  $k_w$  can be anticipated through the function  $f(\mathcal{W})$ .

Equation (23) anticipates the weak dependence of the model output (i.e. either the plume height or the source mass flux) on the magmatic tempera-

Table 9: The change in the source mass flux  $Q_0$  (measured in kg/s) inferred from the plume height when the specified magmatic temperature  $T_0$  (K) is changed by  $\pm 100$  K for each of the eruption scenarios. The other model inputs are held fixed at their reference values.

Eruption scenario	$T_0$	$Q_0$ for $T = T_0$	$Q_0$ for $T = T_0 + 100$ (% change)	$Q_0$ for $T = T_0 - 100$ (% change)
Weak eruption with wind	1273	$1.08 \times 10^7$	$9.50 \times 10^6$ (-12%)	$1.23 \times 10^7$ (+14%)
Weak eruption without wind	1273	$1.94 \times 10^5$	$1.72 \times 10^5$ (-11%)	$2.21 \times 10^5$ (+14%)
Strong eruption with wind	1053	$1.81 \times 10^9$	$1.38 \times 10^9$ (-23%)	$2.90 \times 10^9$ (+60%)
Strong eruption without wind	1053	$8.71 \times 10^8$	$6.84 \times 10^8$ (-21%)	$1.28 \times 10^9$ (+47%)

ture,  $T_0$ , and the source gas mass fraction,  $n_0$ . Indeed, equation (23) suggests that these thermodynamics variables influence the plume properties through the difference in internal energy between the eruption column and the atmosphere relative to the internal energy of the atmosphere. The variations of the source gas mass fraction  $n_0$  (table 1) alone change the bulk heat capacity at the vent by only  $\pm 1\%$ , so do not result in significant changes to the heat content of the plume at the vent. The variations in  $T_0$  alone result in changes of approximately  $\pm 8\%$  to the heat content at the vent. Taken together, variations in  $T_0$  and  $n_0$  change the heat content of the plume at the vent by  $\pm 10\%$ . Equation (23) then suggests the source mass flux would vary by approximately  $\pm 10\%$  when the magmatic temperature changes by  $\pm 100$  K (approximately  $\pm 10\%$  of the reference temperature) for a fixed plume height. While this is consistent with the model solutions for the weak eruption scenario, changes in the source temperature have a greater effect for the strong eruption (table 9). This suggests that changes in the source temperature have an important effect on the plume dynamics that is not captured by equation (23).

Examining profiles of properties of the plume for the strong eruption scenario (figure 15) for different values of the source temperature, we note that changing the source temperature results in significant changes to the vertical velocity profile. While all three of the plumes in figure 15 are super-buoyant (i.e. there is an acceleration phase as the column becomes buoyant above the vent, Woods 1988), the low source temperature results in a significantly lower velocity in the lower part of the plume. This reduces the entrainment of ambient air (as, in this weak wind field, the entrainment is approximately linearly proportional to vertical velocity) and therefore the temperature in the plume is reduced less rapidly (figure 15). The plume with low source

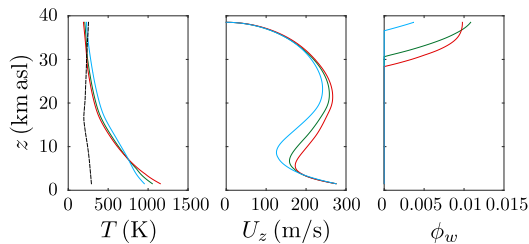


Figure 15: Profiles of the plume temperature,  $T$ , vertical velocity,  $U_z$ , and mass fraction of liquid water,  $\phi_w$ , as functions of height for the strong eruption with wind included and a specified plume top height of 38.5 km asl. Three values of the source temperature are specified:  $T_0 = 953$  K (blue),  $T_0 = 1053$  K (green) and  $T_0 = 1153$  K (red). The black dashed line shows the temperature profile of the ambient atmosphere.

temperature can therefore heat entrained air to greater heights, remaining buoyant when the higher source temperature plumes have becoming negatively buoyant. This behaviour is not found for the weak eruption scenario, where the plume is not super-buoyant and changes to the source temperature do not substantially alter the vertical velocity profiles (not shown).

The exit velocity is not included in equation (23). However, models of pure plumes with a source momentum flux (known as forced plumes) suggest that the evolution in the momentum-driven jet region does not strongly influence the behaviour beyond a few source radii downstream of the vent. For plumes that become buoyant, the jet-like region typically represents a small proportion of the total rise height of the plume (Woods, 1988), and the exit velocity is therefore not expected to strongly affect the rise height of the plume. However, the exit velocity is important in determining whether the eruption column becomes buoyant or collapses (Woods, 1988; Sparks et al., 1997; Degruyter and Bonadonna, 2013).

Degruyter and Bonadonna (2013) identify two dimensionless parameters then allow a regime diagram for buoyant and collapsing eruption columns to be constructed. For plume rising in a quiescent atmosphere, the transition from buoyant to collapsing plumes is determined by the condition (Degruyter and Bonadonna, 2013)

$$\Gamma_1 > \Gamma_{1c}, \quad \text{where } \Gamma_1 = - \left( \frac{\rho_{A0} - \rho_0}{\rho_{A0}} \right) \left( \frac{Q_0}{\pi \rho_0 U_0} \right)^{1/2} \frac{g}{k_s U_0^2}, \quad (27)$$

and where  $\Gamma_{1c}$  is a threshold whose value depends on the remaining source

conditions, with typical values of 5–10 (Degruyter and Bonadonna, 2013). In a windy atmosphere, the parameter  $\Gamma_2 = k_w V / k_s U_0$  is defined, and the buoyant/collapsing regimes are separated by a curve that is approximated as

$$\frac{\Gamma_1}{\Gamma_{1c}} = 1 + \frac{\Gamma_2}{\Gamma_{2c}}, \quad (28)$$

with collapsing plumes to the right of this curve in the  $(\Gamma_1, \Gamma_2)$ -plane, and where the value of  $\Gamma_{2c} \approx 0.6$  is weakly dependent on the source condition (Degruyter and Bonadonna, 2013).

From these transition criteria, the occurrence of the collapsing columns found in the global sensitivity analysis of the strong eruption case can be understood. When the wind is removed from the atmospheric profiles, the criterion (27) indicates that collapsing plumes will occur for high source mass flux, low exit velocity and low values of the no-wind entrainment coefficient, to give values of  $\Gamma_1$  exceeding the threshold value. These dependencies are observed in figures 13 and 14.

When the wind is included in the atmospheric profiles, the criterion (28) suggests additional dependencies on the wind entrainment coefficient  $k_w$ , the magmatic temperature  $T_0$  and the exsolved gas fraction  $n_0$  (which affect the plume density at the vent) and the wind speed scale factor  $\lambda$ . These dependencies are observed in figures 10, 11 and 12. Figure 16 illustrates the buoyant and collapsing plume regimes for a sample 500 source conditions and parameter values in the strong eruption case, plotted on the  $\Gamma_1$ - $\Gamma_2$  plane. The criterion (28) with  $\Gamma_{1c} = 5$  adequately describes the transition in regimes.

For the atmospheric conditions considered in the two scenarios of this study, the moisture content of the plume does not strongly influence the dynamics. Indeed, for the strong plume case, some of the highest rising plumes found in our sampling of the model input space do not have a phase change of water vapour occurring. When condensation does occur in the plumes for the strong eruption it is likely that latent heat of condensation provides only a small proportion of the total energy of the plume. In the weak eruption case, we observe that the highest plumes in our sampling have a phase change of water occurring during the ascent. However, the relative humidity of the atmosphere is less than 35% for this scenario, so little moisture is entrained from the atmosphere. In other settings, the influence of moisture can be much greater (Woods, 1993; Glaze et al., 1997; Mastin, 2007; Woodhouse et al., 2013), and modelling the condensation of water vapour is important to understand other processes that occur in the plume

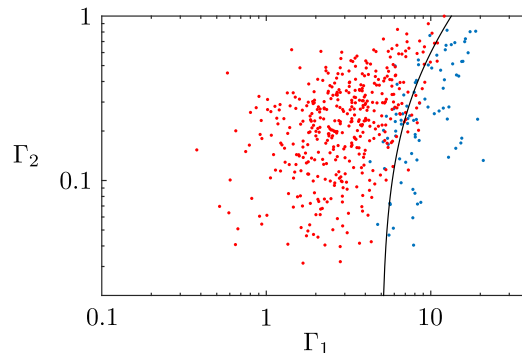


Figure 16: Regime diagram for buoyant (red) and collapsing (blue) plumes. Source conditions, parameter values and atmospheric conditions for the strong plume case are adopted. The curve  $\Gamma_1 = 5(1 + \Gamma_2/0.6)$  well describes the transition between conditions that result in buoyant plumes and those leading to column collapse.

such as lightning (e.g. Behnke et al., 2014; Woodhouse and Behnke, 2014) and aggregation of ash (e.g. Brown et al., 2012; Van Eaton et al., 2012, 2015).

### 5.1. Analyses of sensitivity and uncertainty

The analyses conducted in this study provide insight into the sensitivity of the model output to variations in the inputs to the model. This is an important component of an uncertainty analysis. The sensitivity analysis can be used to identify those inputs whose uncertainty must be included and propagated through the model when comparing predictions to observations. However, there are other essential requirements of an uncertainty analysis.

Uncertainties in making measurements of physical processes in the environment can be significant and these observational uncertainties must be quantified and included when models are applied to draw inferences from observations. Furthermore, idealisations in the model introduce uncertainties, known as structural uncertainties, and these must also be quantified and included in uncertainty analyses (Woodhouse et al., 2015). A crucial component of this is quantifying the influence of physical processes that are not included in the model (Woodhouse et al., 2015). The comparison of the results of sensitivity analyses applied to models that include different physical processes is a useful approach to quantifying structural uncertainty.

Global sensitivity analyses, where model inputs are simultaneously varied across their domains, are crucial as one-at-a-time sensitivity analyses do not

fully explore connections between variables (Saltelli et al., 2008). For example, this study demonstrates that while variations in the source temperature alone can have a pronounced effect, when uncertainty in other model inputs are also considered, the models outputs are less sensitive to the source temperature than the source mass flux and entrainment coefficients. However, the analysis performed here is a partial sensitivity analysis, with the model boundary conditions and a subset of the model parameters varied. In particular, the thermodynamic parameters (heat capacities of the constituent phases) are not changed from default values, but the values of these parameters are uncertain in volcanic settings. Furthermore, variations in one of the source temperature, gas mass fraction and heat capacities can be offset by changes in another of these inputs. Therefore, it is unlikely that an inversion study using uncertain observations of the plume height could be used to predict the source temperature or volatile content (Woodhouse et al., 2015).

Often uncertainty analyses adopt a Bayesian statistical approach (e.g. Kennedy and O’Hagan, 2001; Craig et al., 2001), constructing posterior probability distributions by refining specified prior distributions using observations (see e.g. Denlinger et al., 2012; Anderson and Segall, 2013; Madankan et al., 2014). For a model with a large number of inputs, the calculation of the posterior probability distribution can be computationally demanding. Woodhouse et al. (2015) demonstrates an alternative approach to uncertainty analysis, known as history matching, that can be performed in a similar way to the global sensitivity analysis conducted in this study. The values of uncertain model inputs are sampled from defined prior distributions using a space-filling Latin hypercube design to propagate their uncertainty through the model. The model outputs are then assessed against observations by defining implausibility measures that incorporate observational, parameter and structural uncertainties (Vernon et al., 2010; Woodhouse et al., 2015). In both the Bayesian calibration and history matching uncertainty analyses, preliminary sensitivity analyses are extremely valuable as non-influential parameters can be eliminated, even if there is substantial uncertainty in their values (Woodhouse et al., 2015).

## 6. Conclusions

We have conducted a global sensitivity analysis of the PlumeRise model of moist, wind-blown volcanic plumes. The dependence of the model output to variations in the conditions representing the volcanic source and a subset

of the model parameters is examined in two eruption scenarios. Our analysis shows that the model predictions are most sensitive to the values specified for the source mass flux (in forward model computations) or the plume height (when a model inversion is performed to estimate the source mass flux) and to the entrainment coefficients. Variance-based sensitivity indices can be used to quantify the dependence of the model to its inputs, but these can be misleading when the distribution of the model output is multi-modal, as found here for the strong eruption scenario when column collapse can occur. Visualisation of the model input and output space through parallel coordinate plots is an effective tool for examining the model sensitivities.

This work has been conducted as part of an inter-comparison of models of volcanic plumes. By examining the predictions and sensitivity of different models in this structured exercise, the results can be used to learn about the sources of structural uncertainty in the models and to quantify these uncertainties.

### **Acknowledgements**

We thank Prof. J.C. Rougier for guidance on the analysis of uncertainty in models applied to the natural environment. We are grateful to Dr. M. de' Michieli Vitturi and an anonymous reviewer for suggestions that have improved the manuscript and to Dr. A. Costa for handling the submission. The authors have received funding from the Natural Environment Research Council through the Vanaheim project, "Characterisation of the Near-Field Eyjafjallajökull Volcanic Plume and its Long-range Influence" (NE/I01554X/1), and from the European Union Seventh Framework Programme (FP7, 2007-2013) under grant agreement number 308377, FutureVolc. MJW and JCP also received support from the Natural Environment Research Council Consortium on Risk in the Environment: Diagnostics, Integration, Benchmarking, Learning and Elicitation (CREDIBLE) (NE/J017450/1).

### **Appendix A. Visualizing multivariable data using parallel coordinates plots**

Parallel coordinates plots are a powerful visualization technique for multivariable data and are widely used in sensitivity analyses (for example, the SAFE toolbox (Pianosi et al., 2015) for performing and examining sensitivity analyses in Matlab includes a parallel coordinates plotting routine). The

mathematical foundations of parallel coordinates is well-established (see Inselberg, 1985, 2009), and there are numerous papers on the application and extension of the methodology to a variety of problems in data analysis, data mining and visualization.

The basic parallel coordinates plot consists of a set of line segments connecting vertices that are placed on a sequence of parallel aligned coordinate axes; such a visualization is easy to construct. However, for large data sets that are typically required to explore the sensitivity of a model with a large number of input variables, a simple parallel coordinates plot can appear to be a complicated web of tangled lines weaving across the coordinate axes. Examining parallel coordinates plots for simple example functions, where the dependence of the variables is clear, allows us to identify patterns and so to make inferences in applications for which the underlying functional form is not known explicitly. Figure A.17 shows examples of parallel coordinates plots for eight functions of a single variable,  $y = f(x)$ . On a parallel coor-

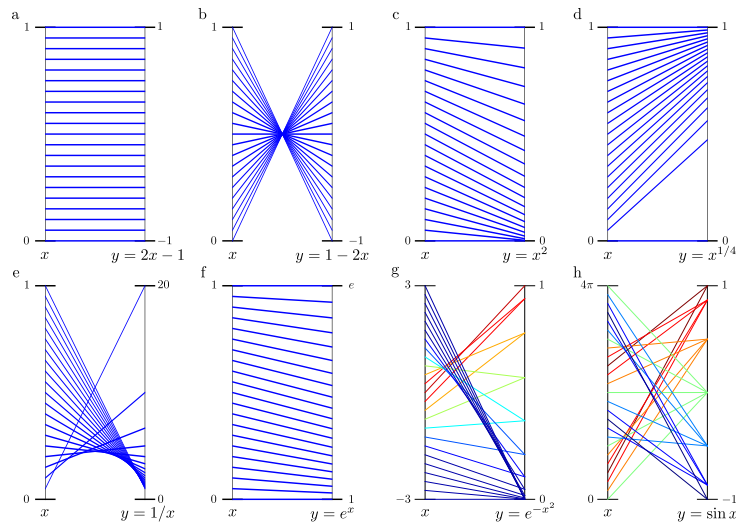


Figure A.17: Parallel coordinate plots for functions of one variable  $y = f(x)$ , with (a)  $f(x) = 2x - 1$  for  $x \in [0, 1]$ , (b)  $f(x) = 1 - 2x$  for  $x \in [0, 1]$ , (c)  $f(x) = x^2$  for  $x \in [0, 1]$ , (d)  $f(x) = x^{1/4}$  for  $x \in [0, 1]$ , (e)  $f(x) = 1/x$  for  $x \in (0, 1]$ , (f)  $f(x) = e^x$  for  $x \in [0, 1]$ , (g)  $f(x) = e^{-x^2}$  for  $x \in [-3, 3]$ , (h)  $f(x) = \sin x$  for  $x \in [0, 4\pi]$ . Colour is used in (g) and (h) to highlight the symmetry and periodicity, respectively, of the output  $y$ .

dinates plot, a linear function with positive slope is represented by parallel lines that are orthogonal to the axes when the  $y$ -axis is scaled to be the same length as the  $x$ -axis (figure A.17a, Inselberg 1985) which is typical on

parallel coordinates plots. In contrast, a linear function with negative slope is represented on a parallel coordinates plot by a sequence of lines that all cross at a single point (figure A.17b, Inselberg 1985). Power-law functions  $y = x^r$ , such as  $y = x^2$  (figure A.17c),  $y = x^{1/4}$  (figure A.17d) and  $y = 1/x$  (figure A.17e), are identified on parallel coordinate plots using the separation between neighbouring line segments; two line segments initiating at  $x_0$  and  $x_0 + \delta x$  on the  $x$ -axis are separated by  $\delta y \approx r x_0^{r-1} \delta x$  on the  $y$ -axis. An exponential function appears similar to a power-law function on a parallel coordinates plot (figure A.17f), however, for two line segments initiating at  $x_0$  and  $x_0 + \delta x$  on the  $x$ -axis, the separation on the  $y$ -axis is  $\delta y \approx e^{x_0} \delta x$ . The exponential function can, of course, be very easily distinguished from a power-law function by transforming a linear  $y$ -axis into a logarithmically scaled axis.

The use of colour to distinguish lines greatly aides the visualization of some functions. For example, for a function that is symmetric about some point on the  $x$ -axis, colouring the line segments by the value of  $y = f(x)$  highlights the symmetry (e.g. figure A.17g illustrates a parallel coordinates plot for a Gaussian function,  $f(x) = e^{-x^2}$ ). Similarly, the identification of a periodic function (such as  $y = \sin x$ , as shown in figure A.17h) is much easier when line segments are coloured according to the value of  $y$ . Colour is particularly useful when there are several coordinate axis, as close neighbours on one pair of the axes can be distinguished if they diverge on another of the axes. When a continuous colour scale that is tied to one of the model inputs or outputs is used to colour line segments it is possible to reduce by one the number of coordinate axes. However, in our study we retain the coordinate axis that is also used to colour the line segments.

Colour can also be usefully applied categorically on parallel coordinates plots. For example, in our study we might be interested in identifying the source conditions that result in plumes rising above 10, km, so could highlight those line segments where the model prediction for the plume height exceeds 10 km in a different colour from the other model results. Further alteration of the properties of the lines can be used to convey additional information. For example, transparency of the line segments greatly aides the visualization of very large data sets. For additional extensions of the parallel coordinates visualization see e.g. Heinrich and Weiskopf (2013).

A great benefit of parallel coordinates plots is their ability to convey information on the interconnections between model variables and assess the combined influence of variations in several inputs on the predictions of a

model. Furthermore, several model outputs can be examined together (e.g. in our study we examine the sensitivity of both the plume height and condensation height to variations in the model inputs). The ‘first-order’ sensitivity of a model output to one of the model inputs is most easily examined when the axis for the model input of interest is a neighbour of the axis along which the model output is plotted. This can only be achieved for all of the model inputs by permuting the axes (Wegman, 1990). ‘Second order’ interactions (i.e. the influence of combined variations in a pair of model inputs on an output) can be easily visualized by arranging the axes so that the two inputs of interest and the model output are grouped together. This also requires permuting the axes in order to examine all possible second-order interactions.

Parallel coordinates plots are particularly easy to interpret when there is a monotonic and nearly linear relationship between the model inputs and the model output. However, we find that nonlinear relationships can also be identified in parallel coordinate plots. Using the example function

$$y = f(x_1, x_2) = \left(x_1 - \frac{1}{2}\right)^2 + 0.1x_2, \quad (\text{A.1})$$

with  $0 \leq x_1, x_2 \leq 1$ , (suggested to us by Dr. M. de’ Michieli Vitturi) we anticipate a strong nonlinear dependence of  $y$  on the input  $x_1$  and a weaker linear dependence of  $y$  on  $x_2$ . These dependencies are seen in scatter plots (figure A.18). The dependencies of the model output  $y$  and the sensitivity to

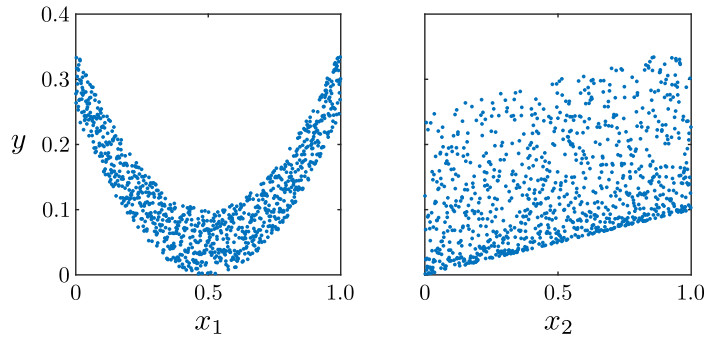


Figure A.18: Scatter plots for the function  $y = \left(x_1 - \frac{1}{2}\right)^2 + 0.1x_2$  for  $0 \leq x_1, x_2 \leq 1$ , with a sample of size 1000 from a Latin hypercube design.

variation in the inputs  $(x_1, x_2)$  can also be observed in a parallel coordinates plot (figure A.19). The non-monotonic dependence of  $y$  on  $x_1$  can be easily

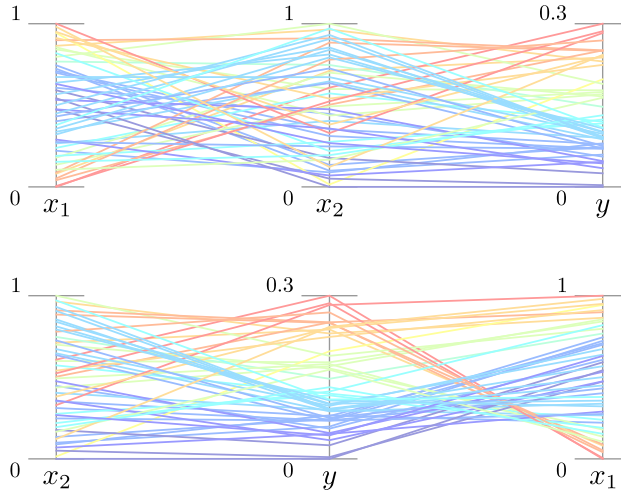


Figure A.19: Parallel coordinates plot for the function  $y = (x_1 - \frac{1}{2})^2 + 0.1x_2$  for  $0 \leq x_1, x_2 \leq 1$ , with a sample of size 50 from a Latin hypercube design. Line segments are coloured by the value of the model output  $y$ .

identified, with trajectories for both  $x_1 \approx 0$  and  $x_1 \approx 1$  linking to relatively large values of  $y$ . The dependence of  $y$  on  $x_1$  is symmetric about the mid-point value for  $x_1$  (i.e.  $x_1 = 1/2$ ) since the colouring of lines on the  $x_1$ -axis is symmetric about the mid-point. Thus, with further analysis (e.g. changing the colour scale from linear to quadratic etc.) one might be able to learn more about the nonlinear form of the function. The weak dependence of the output  $y$  on  $x_2$  (i.e. low sensitivity to  $x_2$ ) can be inferred from the unclear pattern of trajectories through the  $x_2$ -axis.

The example function (A.1) is of a particularly simple form; the functional dependencies on  $x_1$  and  $x_2$  occur separably. In general, of course, this is not expected, and to illustrate this point we analyse a different example function with non-separable dependencies. Identifying interactions between model inputs is a particular strength of the parallel coordinates visualization. A second example function, a modification of (A.1) to include an interaction term, can be used to demonstrate this. We take a function

$$y = f(x_1, x_2, x_3) = (x_1 - \frac{1}{2})^2 + 0.1x_2 + \frac{1}{4}(1 - \tanh(10x_1)) \cos(\pi x_3), \quad (\text{A.2})$$

with  $0 \leq x_i \leq 1$  for  $i = 1, 2, 3$ , noting that the interaction term has a form such that the new input  $x_3$  contributes when  $x_1 \approx 0$  and most substantially

when  $x_3 \approx 0$ . The scatter plots for this function are shown in figure A.20. From the scatter plots we infer (i) that the output  $y$  is most sensitive to the

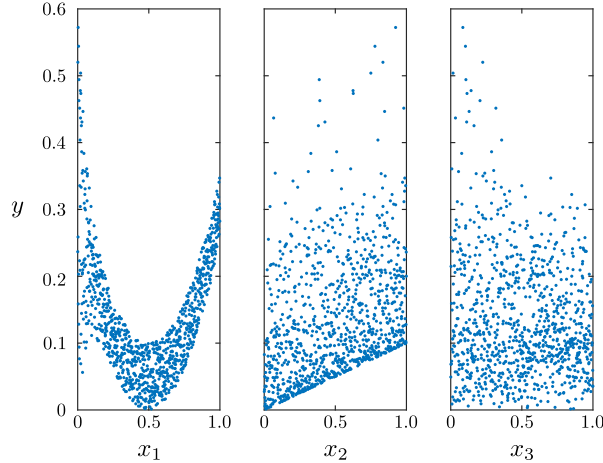


Figure A.20: Scatter plots for the function  $y = (x_1 - \frac{1}{2})^2 + 0.1x_2 + \frac{1}{4}(1 - \tanh(10x_1)) \cos(\pi x_3)$  with  $0 \leq x_i \leq 1$  for  $i = 1, 2, 3$ , with a sample of size 1000 from a Latin hypercube design.

value of  $x_1$  and (ii) that there is similar sensitivity to  $x_2$  and  $x_3$ . However, it is difficult to determine inter-connections between the inputs, although some interaction between  $x_1$  and  $x_3$  can be anticipated for  $x_1 \approx 0$  and  $x_3 \approx 0$ . If we examine a parallel coordinates plot for this function, shown in figure A.21, the strong nonlinear dependence of  $y$  on  $x_1$  is apparent, with much less sensitivity to the other inputs. We can further examine the interactions by tracing trajectories across the axes. We see, for example, that the three largest values of  $y$  occur for  $x_1 \approx 0$  and  $x_3$  taking relatively low values, and, furthermore, that there is a clear ordering with  $y$  increasing as  $x_3$  decreases with  $x_1 \approx 0$ . We also note that when  $x_1 \approx 1$  there is no discernible dependence of  $y$  on  $x_3$ .

We note also that the inferences drawn using parallel coordinates plots can be made with many fewer model evaluations than the scatter plots. For example, if we examine the scatter plots for the example function (A.2) using the same 50 sample points as used in the parallel coordinates plot (figure A.22) then it is difficult to draw firm conclusions. For these example functions (and for our plume model) the computational cost is small, so that many evaluations can be made, but for computationally expensive models

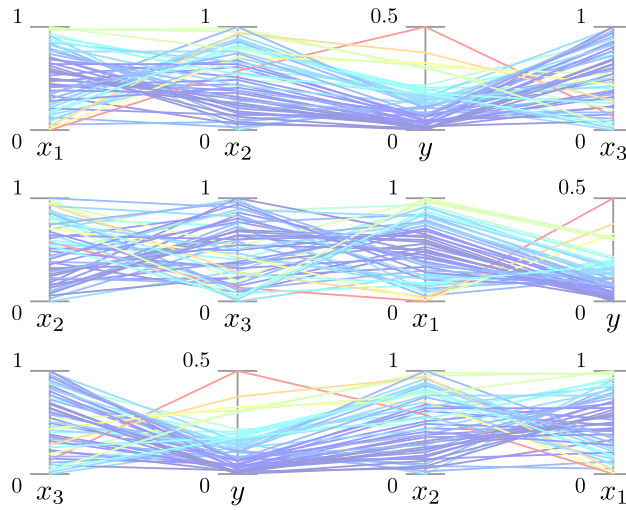


Figure A.21: Parallel coordinates plot for the function  $y = (x_1 - \frac{1}{2})^2 + 0.1x_2 + \frac{1}{4}(1 - \tanh(10x_1))\cos(\pi x_3)$  with  $0 \leq x_i \leq 1$  for  $i = 1, 2, 3$ , with a sample of size 50 from a Latin hypercube design. Line segments are coloured by the value of the model output  $y$ .

there is a great advantage in visualizations that allow detailed analyses but require few evaluations.

Alduchov, O. A., Eskridge, R. E., 1996. Improved Magnus form approximation of saturation vapor pressure. *J. Appl. Meteorol.* 35, 601–609.

Anderson, K., Segall, P., 2013. Bayesian inversion of data from effusive volcanic eruptions using physics-based models: Application to Mount St. Helens 2004–2008. *J. Geophys. Res. - Solid Earth* 118 (5), 2017–2037.

Archer, G. E. B., Saltelli, A., Sobol', I. M., 1997. Sensitivity measures, ANOVA-like techniques and the use of bootstrap. *J. Stat. Comput. Sim.* 58 (2), 99–120.

Behnke, S. A., Thomas, R. J., Edens, H. E., Krehbiel, P. R., Rison, W., 2014. The 2010 eruption of Eyjafjallajökull: Lightning and plume charge structure. *J. Geophys. Res. - Atmos.* 119.

Brown, R. J., Bonadonna, C., Durant, A. J., 2012. A review of volcanic ash aggregation. *Phys. Chem. Earth* 45-46, 65–78.

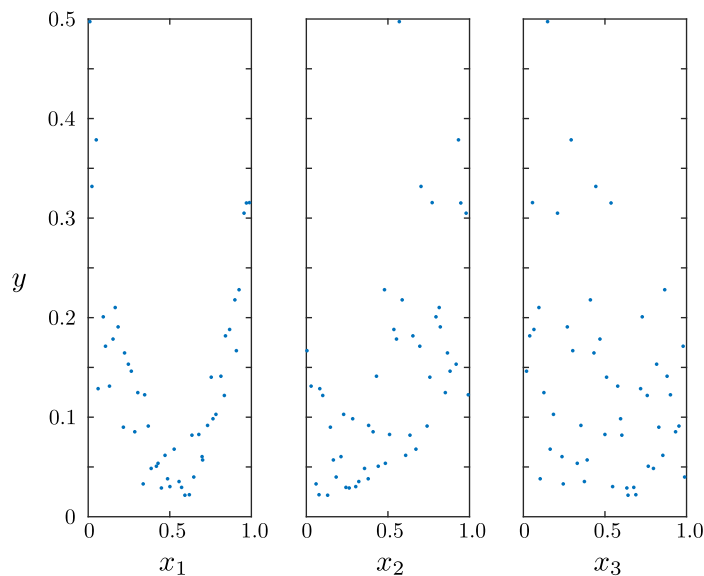


Figure A.22: Scatter plots for the function  $y = (x_1 - \frac{1}{2})^2 + 0.1x_2 + \frac{1}{4}(1 - \tanh(10x_1))\cos(\pi x_3)$  with  $0 \leq x_i \leq 1$  for  $i = 1, 2, 3$ , with a sample of size 50 from a Latin hypercube design.

Bursik, M., 2001. Effect of wind on the rise height of volcanic plumes. *Geophys. Res. Lett.* 28 (18), 3621–3624.

Bursik, M. I., Kobs, S. E., Burns, A., Braitseva, O. A., Bazanova, L. I., Melekestsev, I. V., Kurbatov, A., Pieri, D. C., 2009. Volcanic plumes and wind: Jetstream interaction examples and implications for air traffic. *J. Volcanol. Geoth. Res.* 186 (1-2), 60–67.

Carazzo, G., Kaminski, E., Tait, S., 2006. The route to self-similarity in turbulent jets and plumes. *J. Fluid Mech.* 547, 137–148.

Costa, A., Suzuki, Y. J., Cerminara, M., Devenish, B. J., Ongaro, T. E., Herzog, M., Eaton, A. R. V., Denby, L. C., Bursik, M., de’MichieliVitturi, M., Engwell, S., Neri, A., Barsotti, S., Folch, A., Macedonio, G., Girault, F., Carazzo, G., Tait, S., Kaminski, E., Mastin, L. G., Woodhouse, M. J., Phillips, J. C., Hogg, A. J., Degruyter, W., Bonadonna, C., 2016. Results of the eruptive column model inter-comparison study. *J. Volcanol. Geoth. Res.*, –.

- Craig, P. S., Goldstein, M., Rougier, J. C., Seheult, A. H., 2001. Bayesian forecasting for complex systems using computer simulators. *J. Am. Stat. Assoc.* 96 (454), 717–729.
- de' Michieli Vitturi, M., Engwell, S. L., Neri, A., Barsotti, S., This issue. Uncertainty quantification and sensitivity analysis of volcanic columns: results from the integral model PLUME-MoM. *J. Volcanol. Geoth. Res.*
- Degruyter, W., Bonadonna, C., 2012. Improving on mass flow rate estimates of volcanic eruptions. *Geophys. Res. Lett.* 39, L16308.
- Degruyter, W., Bonadonna, C., 2013. Impact of wind on the condition for column collapse of volcanic plumes. *Earth Planet. Sci. Lett.* 377-378, 218–226.
- Denlinger, R. P., Pavolonis, M., Sieglaff, J., 2012. A robust method to forecast volcanic ash clouds. *J. Geophys. Res. - Atmos.* 117, D13208.
- Ernst, G. G. J., Sparks, R. S. J., Carey, S. N., Bursik, M. I., 1996. Sedimentation from turbulent jets and plumes. *J. Geophys. Res.* 101 (B3), 5575–5589.
- Ezzamel, A., Salizzoni, P., Hunt, G. R., 2015. Dynamical variability of axisymmetric buoyant plumes. *J. Fluid Mech.* 765, 576–611.
- Folch, A., Costa, A., Macedonio, G., 2015. FPLUME-1.0: An integrated volcanic plume model accounting for ash aggregation. *Geosci. Model Dev. Discuss.* 8, 8009–8062.
- Gill, A. E., 1982. *Atmosphere–Ocean Dynamics*. International Geophysics Series. Academic Press.
- Glaze, L. S., Baloga, S. M., 1996. Sensitivity of buoyant plume heights to ambient atmospheric conditions: Implications for volcanic eruption columns. *J. Geophys. Res.* 101 (D1), 1529–1540.
- Glaze, L. S., Baloga, S. M., Wilson, L., 1997. Transport of atmospheric water vapor by volcanic eruption columns. *J. Geophys. Res.* 102 (D5), 6099–6108.
- Heinrich, J., Weiskopf, D., 2013. State of the Art of Parallel Coordinates. In: Sbert, M., Szirmay-Kalos, L. (Eds.), *Eurographics 2013 - State of the Art Reports*. The Eurographics Association.

- Hewett, T. A., Fay, J. A., Hoult, D. P., 1971. Laboratory experiments of smokestack plumes in a stable atmosphere. *Atmos. Environ.* 5 (9), 767–772.
- Inselberg, A., 1985. The plane with parallel coordinates. *The Vis. Comput.* 1 (2), 69–91.
- Inselberg, A., 2009. *Parallel Coordinates: Visual Multidimensional Geometry and Its Applications*. Springer, New York.
- Jenkins, S., Wilson, T., Magill, C., Miller, V., Stewart, C., Marzocchi, W., Boulton, M., Blong, R., Bonadonna, C., Costa, A., 2015. Global volcanic hazards and risk. In: Loughlin, S. C., Sparks, S., Brown, S. K., Jenkins, S. F., Vye-Brown, C. (Eds.), *Global Volcanic Hazards and Risk*. Cambridge University Press, Ch. Volcanic ash fall hazard and risk.
- Kaminski, E., Tait, S., Carazzo, G., 2005. Turbulent entrainment in jets with arbitrary buoyancy. *J. Fluid Mech.* 526, 361–376.
- Kaye, N. B., 2008. Turbulent plumes in stratified environments: A review of recent work. *Atmos. Ocean* 46 (4), 433–441.
- Kennedy, M. C., O’Hagan, A., 2001. Bayesian calibration of computer models. *J. Roy. Stat. Soc. B Stat. Methodol.* 63 (3), 425–464.
- Koyaguchi, T., Woods, A. W., 1996. On the formation of eruption columns following explosive mixing of magma and surface-water. *J. Geophys. Res.* 101 (B3), 5561–5574.
- Linden, P. F., 2000. Convection in the environment. In: Batchelor, G. K., Moffatt, H. K., Worster, M. G. (Eds.), *Perspectives in Fluid Dynamics*. Cambridge University Press.
- Madankan, R., Pouget, S., Singla, P., Bursik, M., Dehn, J., Jones, M., Patra, A., Pavolonis, M., Pitman, E. B., Singh, T., Webley, P., 2014. Computation of probabilistic hazard maps and source parameter estimation for volcanic ash transport and dispersion. *J. Comput. Phys.* 271, 39–59.
- Mastin, L. G., 2007. A user-friendly one-dimensional model for wet volcanic plumes. *Geochem. Geophys. Geosyst.* 8 (3), Q03014.

- Mastin, L. G., Guffanti, M., Servranckx, R., Webley, P., Barsotti, S., Dean, K., Durant, A., Ewert, J. W., Neri, A., Rose, W. I., Schneider, D., Siebert, L., Stunder, B., Swanson, G., Tupper, A., Volentik, A., Waythomas, C. F., 2009. A multidisciplinary effort to assign realistic source parameters to models of volcanic ash-cloud transport and dispersion during eruptions. *J. Volcanol. Geoth. Res.* 186 (1-2), 10–21.
- Morris, M. D., Mitchell, T. J., 1995. Exploratory designs for computational experiments. *J. Stat. Plan. Inference* 43 (3), 381–402.
- Morton, B. R., 1957. Buoyant plumes in a moist atmosphere. *J. Fluid Mech.* 2, 127–144.
- Morton, B. R., Taylor, G., Turner, J. S., 1956. Turbulent gravitational convection from maintained and instantaneous sources. *P. Roy. Soc. Lond. A Math. Phys. Eng. Sci.* 234 (1196), 1–23.
- Ogden, D. E., Glatzmaier, G. A., Wohletz, K. H., 2008a. Effects of vent overpressure on buoyant eruption columns: Implications for plume stability. *Earth Planet. Sci. Lett.* 268 (3-4), 283–292.
- Ogden, D. E., Wohletz, K. H., Glatzmaier, G. A., Brodsky, E. E., 2008b. Numerical simulations of volcanic jets: Importance of vent overpressure. *J. Geophys. Res. - Solid Earth* 113, B02204.
- Papanicolaou, P. N., List, E. J., 1988. Investigations of round vertical turbulent buoyant jets. *J. Fluid Mech.* 195, 341–391.
- Pianosi, F., Sarrazin, F., Wagener, T., 2015. A Matlab toolbox for Global Sensitivity Analysis. *Environ. Model. Softw.* 70, 80–85.
- Press, W. H., Teukolsky, S. A., Vetterling, W. T., Flannery, B. P., 2007. *Numerical Recipes*, 3rd Edition. Cambridge University Press, Cambridge.
- Rogers, R. R., Yau, M. K., 1989. *A Short Course in Cloud Physics*, 3rd Edition. Pergamon Press, Oxford.
- Saffaraval, F., Solovitz, S. A., Ogden, D. E., Mastin, L. G., 2012. Impact of reduced near-field entrainment of overpressured volcanic jets on plume development. *J. Geophys. Res. - Solid Earth* 117, B05209.

- Saltelli, A., Annoni, P., Azzini, I., Campolongo, F., Ratto, M., Tarantola, S., 2010. Variance based sensitivity analysis of model output. Design and estimator for the total sensitivity index. *Comput. Phys. Commun.* 181 (2), 259–270.
- Saltelli, A., Ratto, M., Andres, T., Campolongo, F., Cariboni, J., Gatelli, D., Saisana, M., Tarantola, S., 2008. *Global Sensitivity Analysis: The Primer*. Wiley.
- Self, S., 2006. The effects and consequences of very large explosive volcanic eruptions. *Philos. Trans. R. Soc. A Math. Phys. Eng. Sci.* 364 (1845), 2073–2097.
- Settle, M., 1978. Volcanic eruption clouds and the thermal power output of explosive eruptions. *J. Volcanol. Geoth. Res.* 3, 309–324.
- Sobol', I. M., 2001. Global sensitivity indices for nonlinear mathematical models and their Monte Carlo estimates. *Math. Comput. Simul.* 55 (1–3), 271–280.
- Sparks, R. S. J., Bursik, M. I., Carey, S. N., Gilbert, J. S., Glaze, L. S., Sigurdsson, H., Woods, A. W., 1997. *Volcanic Plumes*. John Wileys & Sons, Chichester, U.K.
- Van Eaton, A. R., Mastin, L. G., Herzog, M., Schwaiger, H. F., Schneider, D. J., Wallace, K. L., Clarke, A. B., 2015. Hail formation triggers rapid ash aggregation in volcanic plumes. *Nat. Commun.* 6, 7860.
- Van Eaton, A. R., Muirhead, J. D., Wilson, C. J. N., Cimorelli, C., 2012. Growth of volcanic ash aggregates in the presence of liquid water and ice: an experimental approach. *B. Volcanol.* 74 (9), 1963–1984.
- Vernon, I., Goldstein, M., Bower, R. G., 2010. Galaxy formation: a Bayesian uncertainty analysis. *Bayesian Anal.* 5 (4), 619–669.
- Wang, H., Law, A. W.-K., 2002. Second-order integral model for a round turbulent buoyant jet. *J. Fluid Mech.* 459, 397–428.
- Wegman, E. J., 1990. Hyperdimensional data analysis using Parallel Coordinates. *J. Am. Stat. Assoc.* 85 (411), 664–675.

- Wilson, L., Sparks, R. S. J., Huang, T. C., Watkins, N. D., 1978. The control of volcanic column heights by eruption energetics and dynamics. *J. Geophys. Res.* 83 (B4), 1829–1836.
- Woodhouse, M. J., Behnke, S. A., 2014. Charge structure in volcanic plumes: a comparison of plume properties predicted by an integral plume model to observations of volcanic lightning during the 2010 eruption of Eyjafjallajökull, Iceland. *B. Volcanol.* 76 (8).
- Woodhouse, M. J., Hogg, A. J., Phillips, J. C., Rougier, J. C., 2015. Uncertainty analysis of a model of wind-blown volcanic plumes. *B. Volcanol.* 77 (10).
- Woodhouse, M. J., Hogg, A. J., Phillips, J. C., Sparks, R. S. J., 2013. Interaction between volcanic plumes and wind during the 2010 Eyjafjallajökull eruption, Iceland. *J. Geophys. Res. - Solid Earth* 118, 92–109.
- Woods, A. W., 1988. The fluid dynamics and thermodynamics of eruption columns. *B. Volcanol.* 50, 169–193.
- Woods, A. W., 1993. Moist convection and the injection of volcanic ash into the atmosphere. *J. Geophys. Res.* 98 (B10), 17627–17636.
- Woods, A. W., 2010. Turbulent Plumes in Nature. *Annu. Rev. Fluid Mech.* 42, 391–412.
- Woods, A. W., Bower, S. M., 1995. The decompression of volcanic jets in a crater during explosive volcanic eruptions. *Earth Planet. Sci. Lett.* 131 (3–4), 189 – 205.
- Woods, A. W., Bursik, M. I., 1991. Particle fallout, thermal disequilibrium and volcanic plumes. *B. Volcanol.* 53, 559–570.
- Yang, J., 2011. Convergence and uncertainty analyses in Monte-Carlo based sensitivity analysis. *Environ. Model. Softw.* 26 (4), 444–457.